

## Article

# Dynamic strategies for yaw and induction control of wind farms based on large-eddy simulation and optimization

Wim Munters , Johan Meyers 

KU Leuven, Department of Mechanical Engineering, Celestijnenlaan 300A, 3001 Leuven, Belgium

\* Correspondence: wim.munters@kuleuven.be

Academic Editor: name

Version December 7, 2017 submitted to Energies

**Abstract:** In wind farms, wakes originating from upstream turbines cause reduced energy extraction and increased loading variability in downstream rows. The prospect of mitigating these detrimental effects through coordinated controllers at the wind-farm level has fueled a multitude of research efforts in wind-farm control. The main strategies in wind-farm control are to influence the velocity deficits in the wake by deviating from locally optimal axial induction setpoints on the one hand, and steering wakes away from downstream rows through yaw misalignment on the other hand. The current work investigates dynamic induction and yaw control of individual turbines for wind-farm power maximization in large-eddy simulations. To this end, receding-horizon optimal control techniques combined with continuous adjoint gradient evaluations are used. We study a  $4 \times 4$  aligned wind farm, and find that yaw control is more effective than induction control, both for uniform and turbulent inflow conditions. Analysis of optimal yaw controls leads to the definition of two simplified yaw control strategies, in which wake meandering and wake redirection are exploited respectively. Furthermore it is found that dynamic yawing provides significant benefits over static yaw control in turbulent flow environments, whereas this is not the case for uniform inflow. Finally, the potential of combining overinductive axial induction control with yaw control is shown, with power gains that approximate the sum of those achieved by each control strategy separately.

**Keywords:** wind farm, large-eddy simulation, optimal control, adjoint optimization

## 1. Introduction

Complex wake interactions between wind turbines situated in wind farms lead to both decreased energy extraction efficiency and increased loading in downstream rows. The current wind-farm control paradigm however maximizes performance and minimizes loads at the turbine level, and does not take these interactions into account. In recent years, considerable research investigations have been performed into control strategies that aim to mitigate these detrimental effects through coordinated wind-farm control. In the context of this manuscript, we focus on mitigating downstream efficiency losses through wind-farm control. The existing literature on wind-farm control for power maximization exhibits a dichotomy in control strategies between axial induction control and wake redirection control [1]. Both strategies aim at improving the overall wind-farm efficiency by operating upstream turbines at locally non-optimal off-design conditions, altering the flow field through the wind farm such that power gains in downstream regions compensate for upstream efficiency losses. Furthermore, a distinction can be made based on the internal flow model used by the controller, ranging from model-free to control-oriented engineering models and large-eddy simulations (LES). A second classification can be made based on the dynamics of the control law, i.e. static or

dynamic control. The current work is the first investigation into the potential of combining dynamic axial induction and wake redirection control in wind farms using accurate large-eddy simulations modeling tools. Firstly, the current state of the art in wind-farm control is briefly reviewed for both axial induction and wake redirection strategies. A more elaborate overview of the field is given in Refs. [1,2]. Thereafter, the aims of the current work are revisited, and the structure of the manuscript is detailed.

*Axial induction control* aims to alter the induced slowdown of the turbines by deviating their tip speed ratio and/or blade pitch angle from their locally optimal setpoints. This directly translates to variations in power extraction and wake velocity deficit. In the vicinity of these conventional setpoints, the setpoint sensitivity of the power extraction is much smaller than that of the thrust coefficient force, indicating that wake deficits can be reduced significantly with limited deviations in local power extraction [3]. The idea of axial induction control has been around for a long time as e.g. illustrated by the early study of Steinbuch *et al.* [4].

Studies on *static* axial induction control have attempted to increase overall power by statically curtailing upstream wind turbines [2]. Although some studies have indicated gains in the order of up to 5% for selected cases (see, e.g., Refs. [5–7]), others have noted that gains predicted by engineering models were often not reproduced in high-fidelity environments [3]. Nilsson *et al.* [8] performed an LES study of the Lillgrund wind farm, which is characterized by very strong wake interactions and power deficits, and is hence a prime candidate for axial induction control. However, simple static induction control failed to increase wind-farm power, indicating the need for more involved induction control strategies. In addition, recent wind tunnel studies have indicated discrepancies between power gains predicted by engineering models and those observed in the wind tunnel, and have reported no significant power gains beyond measurement uncertainties for static axial induction control [9,10]. Furthermore, it is important to note that most of the studies on wind-farm control are performed in worst-case conditions, i.e. in which neighboring turbines are aligned with the mean wind direction, with maximal wake interaction and potential for coordinated control. Since wind farms are usually designed in such a way that these conditions occur rarely given the annual distribution of wind direction, the gains obtained by coordinated control should be high enough to have an effect on annual farm energy production. The viability of gains reported by many of the abovementioned studies in actual wind-farm conditions is hence questionable.

In a novel alternative approach, Goit and Meyers [11] investigated *dynamic* axial induction control by applying optimal control techniques directly in a high-fidelity LES model using adjoint-based methods. The wind turbines were used as dynamic flow devices acting upon the turbulent ABL flow without *a priori* limiting the accuracy of the model flow physics representation. In this way, turbines were able to engage in active symbiosis with the physics governing the turbulent flow to increase overall power extraction, and energy extraction was increased by 16% for the asymptotic limit of a fully-developed very large wind farm. This approach was also employed in successive studies of wind farms with entrance effects, in which power gains in the order of 20% were achieved [12–14].

*Wake redirection control* aims to steer wakes away from downstream turbines. In practice, this can be achieved either through individual pitch control, tilt control or through yaw control [15]. Notwithstanding the fact that individual pitch control and, to a lesser extent, tilt control both show potential for increasing power and/or reducing loads [16–18], we will focus on wake redirection for power optimization through yaw control in the remainder of this discussion. Although nominally wind turbines are operated such that the rotor is perpendicular to the incoming flow, an intentional yaw misalignment can be used to induce transversal forces on the incoming flow. The opportunity to change inflow conditions for downstream turbines by redirecting upstream wakes has incited a great amount of interest into characterizing the flow behavior of wind turbines in yaw and harnessing the associated deflection for wind-farm control. Clayton and Filby [19] were the first to quantify the wake deflection behind turbines in yaw in an experimental study. Since then, numerous wind-tunnel

83 investigations have further increased the understanding of the wake characteristics behind yawed  
 84 turbines (see, e.g. Refs. [20–22]). Jiménez *et al.* [23] performed an LES study to characterize wake  
 85 deflection of turbines in yaw, and introduced an analytical model to quantify the displacement of  
 86 the wake center. Recently, Howland *et al.* [24] combined numerical simulations with experimental  
 87 measurements and found that counter-rotating vortices shed from the turbine rotor impose a curled  
 88 shape on the deflected wake.

89     Static yaw control, in which upstream turbines intentionally misalign their rotors with incoming  
 90 winds, has been proven as a promising approach to increasing power extraction, in numerical studies  
 91 [25,26], but also in wind-tunnel tests [27,28] and full-scale field measurements [29,30]. Studies  
 92 on dynamic yaw control however are much more scarce. Gebraad *et al.* [31] applied a dynamic  
 93 engineering model in order to incorporate time lag effects due to wake propagation. However, this  
 94 model is unable to capture any turbulent mixing effects that have been shown to hold potential for  
 95 enhanced wake recovery in the context of induction control as shown in Goit and Meyers [11]. The  
 96 possibility of unsteadily yawing turbines interacting with dynamic flow mechanisms has not been  
 97 investigated to date.

98     Furthermore, the combination of axial induction and wake redirection control has remained  
 99 virtually uncharted terrain to date [1]. A notable exception are the studies by Park *et al.* [28,32],  
 100 who employed a model-free data-driven approach for the static control of both yaw and blade pitch  
 101 angles of the individual turbines within the farm. The control optimizer encouraged turbines to  
 102 steadily deviate yaw angle and, to a lesser extent, pitch angles from their greedy setpoints, both in  
 103 a engineering model simulation environment [32,33] and in a wind-tunnel test [28]. However, no  
 104 estimate was made on the surplus gains achieved by incorporating induction control in addition to  
 105 yaw control only, and the model-free approach did not allow for unsteady control interacting with  
 106 the flow dynamics.

107     In the current manuscript, we aim to fill some of the aforementioned gaps in wind-farm  
 108 control research. We extend the dynamic optimal induction control framework SP-Wind [11,14]  
 109 to incorporate dynamic yaw control. Based on a demonstration  $4 \times 4$  wind-farm control case, we  
 110 illustrate the benefits of unsteady yaw control, and uncover the potential of combining yaw control  
 111 with axial induction control. To the best knowledge of the authors, the current manuscript presents  
 112 a first attempt at quantifying the potential of combining the latter control strategies in a dynamic  
 113 manner. The manuscript is structured as follows. Firstly, Section 2 introduces the optimal control  
 114 problem and the numerical methods used to solve it. Next, Section 3 describes the simulation cases,  
 115 and details setup parameters. Thereafter, Section 4 presents optimization results for both uniform and  
 116 turbulent inflow, and identifies distinct yaw control regimes resulting in increased power extraction.  
 117 Finally, Section 5 summarizes the main findings of this manuscript and formulates suggestions for  
 118 future research.

## 119 2. Methodology

120     The simulations presented in this manuscript are performed using the in-house developed optimal  
 121 control framework SP-Wind, which is discussed briefly below. For a more elaborate explanation and  
 122 previous applications of the SP-Wind framework we refer the reader to Refs. [11,12,14,34,35].

123     In a conventional model-predictive optimal-control approach (see Figure 1a), a controller aims  
 124 to maximize the performance of a system (i.e. the wind farm) by optimizing controls based on a  
 125 system state model. Usually, this is done in a receding-horizon framework (see Figure 2), in which  
 126 the state model is optimized over a time window  $[t, t + T]$ , after which the optimal controls  $\varphi^*$  are  
 127 applied to the system for a time period  $T_A < T$ , after which the optimization procedure starts anew.  
 128 Furthermore, in order to mitigate mismatch between the model and the physical system, a state  
 129 estimator provides feedback to the model based on system measurements. However, in a wind-farm  
 130 context, the state of the turbulent atmospheric boundary layer flow is very high dimensional, and  
 131 accurate state models based on the Navier-Stokes equations carry prohibitive computational costs

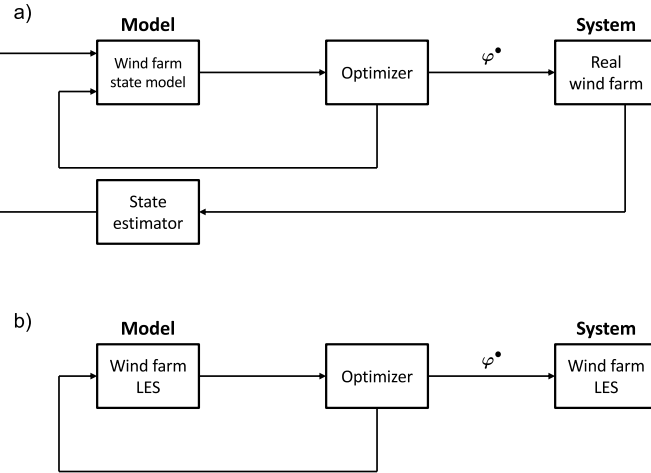


**Figure 1.** Model-predictive control (MPC) applied to wind farms. a) Conventional feedback MPC of a wind farm. b) Benchmark optimal control framework of a wind farm LES considered in the current study. Figure originally published in Munters and Meyers [14] under a CC-BY 4.0 license.

for real-time control implementation. Therefore, computationally affordable engineering models are typically used, relying on simplifying assumptions that limit a priori the performance of the controller.

In contrast, the current manuscript follows the approach first introduced by Goit and Meyers [11]: instead of focusing on developing a practically realizable wind-farm controller, wind-farm performance is optimized directly in an accurate model with full state information, i.e. using large-eddy simulations of the filtered Navier–Stokes equations (see Figure 1b). In this way, instead of being parametrized, the turbulent interactions between wind turbines and the atmospheric boundary layer flow are explicitly resolved using adequate spatio-temporal resolution. In this way, the wind turbines can be used as flow actuators: by dynamically controlling individual thrust setpoints and yaw rates of the turbines we aim to optimally influence the ABL flow such that aggregate wind-farm power extraction is maximized. Note that this approach is unfeasible for practical control, both due to excessive computational cost and the incomplete state information in practice. However, it allows to benchmark the potential of increasing energy through wind-farm control, and can help identify control mechanisms to be harnessed by practical controllers. Also here, a receding-horizon methodology is used. Within each control window, we consider the following PDE-constrained optimal control problem, in which we maximize the aggregate wind-farm power over a time horizon  $T$ :

$$\underset{\varphi, q}{\text{minimize}} \quad \mathcal{J}(\varphi, q) = - \int_0^T \sum_{i=1}^{N_t} \frac{1}{2} C'_{P,i} V_i^3 A_i dt \quad (1)$$

$$\text{s.t.} \quad \frac{\partial \tilde{u}}{\partial t} + (\tilde{u} \cdot \nabla) \tilde{u} = -\nabla(\tilde{p} + \tilde{p}_\infty)/\rho - \nabla \cdot \tau_{sgs} + \sum_{i=1}^{N_t} -\frac{1}{2} \hat{C}'_{T,i} V_i^2 \mathcal{R}_i(x) e_{\perp,i} \quad \text{in } \Omega \times (0, T], \quad (2)$$

$$\nabla \cdot \tilde{u} = 0 \quad \text{in } \Omega \times (0, T], \quad (3)$$

$$\tau \frac{d\hat{C}'_{T,i}}{dt} = C'_{T,i} - \hat{C}'_{T,i} \quad i = 1 \dots N_t \text{ in } (0, T], \quad (4)$$

$$\frac{d\theta_i}{dt} = \omega_i \quad i = 1 \dots N_t \text{ in } (0, T], \quad (5)$$

$$C'_{T,\min} \leq C'_{T,i} \leq C'_{T,\max} \quad i = 1 \dots N_t \text{ in } (0, T], \quad (6)$$

$$-\omega_{\max} \leq \omega_i \leq \omega_{\max}. \quad i = 1 \dots N_t \text{ in } (0, T]. \quad (7)$$

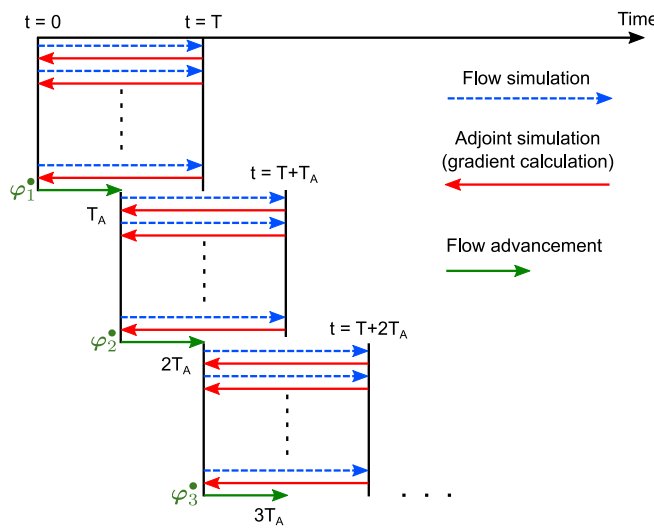


**Figure 2.** Receding horizon framework subdividing time into discrete flow advancement windows of length  $T_A$  with prediction horizon  $T$ . Each arrow represents a forward or adjoint PDE simulation. Each window consists of an optimization stage (blue and red lines), yielding a set of optimal controls  $\varphi^*$ , followed by a flow advancement stage (green line). Figure originally published in Munters and Meyers [14] under a CC-BY 4.0 license.

150  
 151 The ABL state equations in Eq. (2) - (3) are the filtered Navier-Stokes equations, which are solved  
 152 using LES. In these equations,  $\tilde{u}$  and  $\tilde{p}$  are the filtered velocity and modified pressure respectively.  
 153 Furthermore,  $\tau_{sgs}$  is the subgrid-scale stress tensor, which is modeled using a constant-coefficient  
 154 Smagorinsky model. The LES solver applies a Fourier spectral discretization in the horizontal  
 155 directions combined with a energy-conservative fourth order finite-difference scheme in the vertical  
 156 direction. Inflow conditions are specified using a fringe region method [36]. Further details regarding  
 157 the LES solver used in this work can be found for instance in Refs. [37–39].

158 The wind turbines are modeled using a standard non-rotating actuator disk model (see, e.g.,  
 159 Ref [38]). For each turbine  $i (= 1 \dots N_t)$ , two state variables are defined. First, the turbine thrust  
 160 coefficient  $\hat{C}'_{T,i}$  is obtained by applying a one-sided exponential time-filter with time constant  $\tau$  to  
 161 the thrust coefficient control setpoint  $C'_{T,i}$  (Equation 4). Second, the turbine yaw angle  $\theta_i$  is defined  
 162 in a straightforward way using the yaw rate control  $\omega_i$  (Equation 5). Subsequently, the thrust force  
 163 enacted by the turbine upon the flow can be parametrized as  $f_i(x) = -(1/2)\hat{C}'_{T,i}V_i^2\mathcal{R}_i(x)e_{\perp,i}$ . Here,  
 164  $\mathcal{R}_i(x) = \int_{\Omega} G(s-x) H[D/2 - \|s-t_i\|_2] \delta[(s-t_i) \cdot e_{\perp,i}] ds$  is a smoothed geometric footprint of  
 165 the rotor with diameter  $D$  at location  $t_i$  on the LES grid, using a Gaussian kernel  $G$  with characteristic  
 166 filter width  $\Delta$ . Further,  $V_i = (1/A_i) \int_{\Omega} \mathcal{R}_i(x) \tilde{u} \cdot e_{\perp,i} dx$  is the axial velocity averaged over the rotor  
 167 disk with area  $A_i$ , and the rotor-perpendicular unit vector  $e_{\perp,i} = e_x \cos \theta_i + e_y \sin \theta_i$  defines the  
 168 orientation of the rotor disk using the yaw angle state  $\theta_i$ . Analogously, a rotor-parallel unit vector  
 169  $e_{\parallel,i} = -e_x \sin \theta_i + e_y \cos \theta_i$  is defined, which will be used further below. The power extraction of the  
 170 turbine is calculated as  $P_i = (1/2)C'_{P,i}V_i^3A_i$ , with power coefficient  $C'_{P,i} = a\hat{C}'_{T,i}$ . The coefficient in  
 171 the latter linear relation is set to  $a = 0.9$  to mitigate overprediction of turbine power on present-day  
 172 simulation grids as discussed in Ref. [14]. Both the thrust coefficient setpoint controls  $C'_{T,i}$  and the  
 173 yaw rate controls  $\omega_i$  are subjected to technical box constraints in Equations (6) - (7). As discussed  
 174 in Section 3.2 and Table 1, the control cases considered in this manuscript are differentiated based  
 175 on the parameter values of these box constraints. The system states are grouped in the vector  
 176  $q = [\tilde{u}(x,t), \tilde{p}(x,t), \hat{C}'_{T,1}(t), \dots, \hat{C}'_{T,N_t}(t), \theta_1(t), \dots, \theta_{N_t}(t)] = [\tilde{u}(x,t), \tilde{p}(x,t), \hat{C}'_T(t), \theta(t)]$  and the  
 177 controls, consisting of the individual unsteady thrust coefficient setpoints and yaw rates of every  
 178 turbine, are denoted as  $\varphi = [C'_T(t), \omega(t)]$ .

As is common practice in PDE-constrained optimization, the problem is solved in a reduced formulation: the dependency of the state variables on the controls, i.e.  $q(\varphi)$ , is explicitly satisfied by fulfilling the state equations in every step throughout the optimization process, which allows to solve a reduced control-space optimization problem in which the reduced cost functional  $\tilde{\mathcal{J}}(\varphi) \equiv \mathcal{J}(\varphi, q(\varphi))$  is minimized, subject only to the box constraints in equations (6) - (7). The latter problem is solved using the L-BFGS-B algorithm [40], which is an iterative limited-memory quasi-Newton algorithm that uses gradient information to construct and optimize a quadratic model of the cost functional in each iteration while attempting to satisfy the strong Wolfe conditions [41]. As shown in Figure 2, within each optimization window, the iterative procedure hence results in repeated alternating evaluations of the cost functional (i.e. flow simulations using LES) and gradient (i.e. adjoint simulations, see below).

Instead of using a classical finite-difference gradient approximation to determine  $\nabla \tilde{\mathcal{J}}$ , which would require a perturbed LES for every dimension in  $\varphi$  (typically in the order of  $10^4$ – $10^5$ ), the gradient is calculated using the continuous adjoint method. The adjoint methodology is widespread in PDE-constrained optimization since it allows to quantify sensitivities of the cost functional to control parameters at a computational expense independent of control space dimensionality (see, e.g., Refs. [42–45]). The cost functional sensitivity is calculated by deriving and solving an auxiliary set of equations related to the original state equations, called the adjoint equations:

$$-\frac{\partial \xi}{\partial t} + (\nabla \tilde{u})^T \xi - (\tilde{u} \cdot \nabla) \xi = -\nabla \pi / \rho - \nabla \cdot \tau_{sgs}^* + \sum_{i=1}^{N_t} f_i^* \quad \text{in } \Omega \times (0, T] \quad (8)$$

$$\nabla \cdot \xi = 0 \quad \text{in } \Omega \times (0, T] \quad (9)$$

$$-\tau \frac{d\sigma_i}{dt} = -\sigma_i + \frac{1}{2} V_i^2 (aV_i - X_i) A_i \quad i = 1 \dots N_t \text{ in } (0, T] \quad (10)$$

$$\begin{aligned} -\frac{d\eta_i}{dt} &= \frac{1}{2} \hat{C}'_{T,i} V_i \left[ \int_{\Omega} \left( (3V_i - 2X_i) \tilde{u} - V_i \xi \right) \cdot e_{\parallel,i} \mathcal{R}_i dx \right. \\ &\quad \left. + \int_{\Omega} \left( (3V_i - 2X_i) \tilde{u} - V_i \xi \right) \cdot e_{\perp,i} \mathcal{Q}_i dx \right] \quad i = 1 \dots N_t \text{ in } (0, T]. \end{aligned} \quad (11)$$

In these equations  $\xi$ ,  $\pi$ ,  $\sigma_i$ , and  $\eta_i$  are the adjoint variables associated with the state variables  $\tilde{u}$ ,  $\tilde{p}$ ,  $\hat{C}'_{T,i}$ , and  $\theta_i$  from the original optimal control problem. Further,  $X_i$  is the adjoint disk-averaged velocity defined analogously to its forward version  $V_i$ , and  $f_i^* = \frac{1}{2} \hat{C}'_{T,i} V_i (3aV_i - 2X_i) \mathcal{R}_i e_{\parallel,i}$  is the adjoint turbine forcing. The rotational rotor footprint  $\mathcal{Q}_i$  from Equation (11) is defined as

$$\mathcal{Q}_i = \int_{\Omega} \frac{12(s-x) \cdot e_{\perp,i}}{\Delta^2} G(s-x) H[D/2 - \|s-t_i\|_2] \delta[(s-t) \cdot e_{\perp,i}] (s-t_i) \cdot e_{\parallel,i} ds, \quad (12)$$

$$\nabla \tilde{\mathcal{J}} \equiv \begin{bmatrix} \partial \tilde{\mathcal{J}} / \partial C'_T \\ \partial \tilde{\mathcal{J}} / \partial \omega \end{bmatrix} = \begin{bmatrix} -\sigma \\ -\eta \end{bmatrix}. \quad (13)$$

The adjoint gradient expression shown above is derived and compared to a finite difference gradient approximation in Appendix A.

### 3. Numerical setup and case description

This section discusses the simulation cases and setup details that will be used to assess the potential of dynamic yaw control. A wind farm of 16 wind turbines with a rotor diameter  $D = 100$  m is considered. The turbines are arranged in a  $4 \times 4$  aligned pattern, with  $6D$  spacing in both axial and transversal directions. First, numerical setup parameters for the simulation and optimization are discussed. Next, the different control cases are introduced.

210 *3.1. Simulation setup*

211 The simulation domain has a total dimension of  $4.8 \times 2.4 \times 1 \text{ km}^3$ , and is discretized on a grid of  
 212  $256 \times 128 \times 128$  gridpoints. The final 10% of the streamwise extent of the domain is used as a fringe  
 213 region to impose inflow conditions. All cases apply periodic boundary conditions on transversal  
 214 domain boundaries.

215 Two different sets of simulations are considered. The first set is subjected to a steady and uniform  
 216 inflow with  $U_\infty = 8 \text{ m s}^{-1}$ . In this case, the top and bottom boundaries are treated with a symmetry  
 217 condition, and the turbines are placed at the vertical mid-plane  $z_h/H = 0.5$  to minimize any influence  
 218 of vertical domain boundaries. The second set applies unsteady turbulent inflow conditions, which  
 219 are generated in a pressure-driven precursor simulation of an unperturbed turbulent boundary layer  
 220 with shifted periodic boundary conditions [48], driven by a pressure gradient of  $\partial_x p_\infty / \rho = 2.5 \times 10^{-4}$   
 221  $\text{m s}^{-2}$ , resulting in a freestream wind speed at hub height slightly higher than  $8 \text{ m s}^{-1}$ . In this second  
 222 case, the top boundary is treated with a stress-free condition, and a high-Reynolds number wall model  
 223 is used at the bottom. The turbines are placed at a height of  $z_h/H = 0.1$  from the wall. The wall model  
 224 adds a wall stress consistent with a rough-wall logarithmic boundary layer profile with roughness  
 225 length  $z_0/H = 10^{-4}$ , resulting in a inflow turbulence intensity of about 8% at hub height.

226 Within the context of the receding-horizon methodology introduced in Section 2, the  
 227 optimization is performed over 6 time windows. Each window applies an optimization horizon  
 228  $T = 300 \text{ s}$  and a flow advancement time of  $T_A = T/2 = 150 \text{ s}$ , resulting in a total control time  
 229 of  $900 \text{ s}$ . All time-averaged results shown below are based on statistics gathered after  $300 \text{ s}$ , so  
 230 that wake propagation time lag at startup is excluded. To limit computational efforts, we perform  
 231 a fixed amount of 80 L-BFGS-B iterations in each window, corresponding to approximately 160  
 232 PDE simulations (forward or adjoint). Although formal convergence is not achieved for any of the  
 233 cases after this amount of iterations, it will be shown later that the relative ordering of the cases  
 234 based on power extraction is clear. Computational costs amount to approximately 35 000 corehours  
 235 per optimization case for all 6 time windows combined on 112 Intel Broadwell architecture cores  
 236 connected by an EDR Infiniband network. The initial guess for the optimal controls within each  
 237 window is a steady thrust coefficient setpoint  $C'_T = 2$  and yaw rate  $\omega = 0^\circ \text{ s}^{-1}$  for all turbines.  
 238 Simulation and optimization parameters are summarized below in Table 1.

239 Simulations are initialized as follows: for the turbulent inflow case, a fully-developed  
 240 high-Reynolds number turbulent boundary layer is generated in the precursor inflow simulation by  
 241 simulating a perturbed logarithmic flow until a statistically-stationary state is achieved. For both  
 242 the turbulent and the uniform inflow cases the main wind-farm simulation is then advanced in time  
 243 with the proper inflow conditions for approximately five wind-farm flow-through times, after which  
 244 the effects of wind-farm start-up transients have subsided. These statistically stationary wind-farm  
 245 flows then serve as initial conditions for the control cases defined below. Planviews at hub height  
 246 of these initial conditions are shown in Figure 3. It can be seen from the Figure 3a that, given  
 247 laminar inflow conditions, turbine wakes are very deep and remain stable up until row 3, after  
 248 which meandering and vortex shedding starts to occur. These flow conditions can be regarded as  
 249 somewhat artificial since, in the atmospheric boundary layer, background turbulence typically causes  
 250 instant wake transition behind the turbine rotor. Nevertheless, this setup allows us to investigate  
 251 control dynamics more easily, as we can rule out any reaction of the optimization to the background  
 252 variability. Furthermore, suppressed wake meandering and reduced turbulence levels have been  
 253 known to occur in wind farms submerged in stably stratified atmospheric boundary layers [49,50],  
 254 hence rendering the current case somewhat relevant for such situations. Figure 3b shows that, for  
 255 the turbulent inflow case, the background turbulence causes wake instabilities instantly, leading to  
 256 enhanced wake recovery and much more complex unsteady wake interactions between turbines.

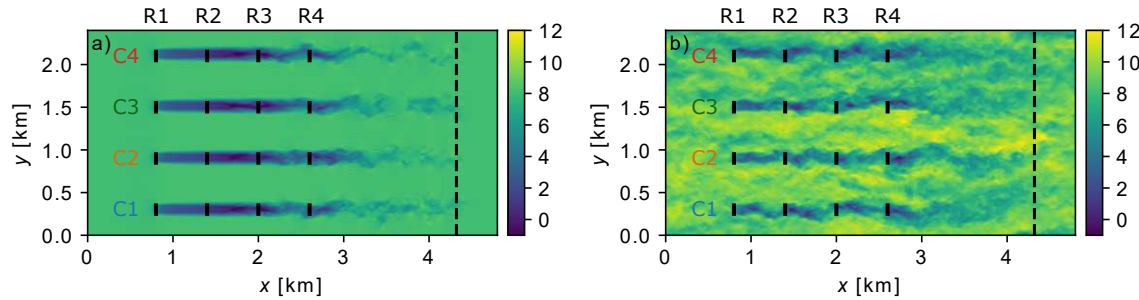


**Figure 3.** Planview at hub height  $z_h$  of initial conditions for optimal control cases. *a)* Uniform and steady inflow. *b)* Turbulent inflow. Colors represent instantaneous streamwise velocity  $\tilde{u}_x$  in  $\text{m s}^{-1}$ . The black lines represent wind turbine locations. The black dashed line indicates the start of the fringe region. R1 – R4 and C1 – C4 indicate the numbering convention used for turbine rows and columns respectively.

### 257 3.2. Control cases

258 For each set of simulations, a steady reference case (R) with  $C'_T = 2$  and  $\omega = 0^\circ/\text{s}$  is considered. In  
 259 this way, turbines in the reference case remain aligned with the mean-flow direction and operate at  
 260 Betz-optimal thrust coefficients. Further, a first yaw control case (Y) is defined, with a steady  $C'_T = 2$ ,  
 261 but turbines are allowed to yaw dynamically at a maximum rate of  $\omega^{\max} = 0.3^\circ/\text{s}$ , corresponding  
 262 to the maximum yaw rate of the conceptual NREL 5MW and the DOWEC 6MW turbines [51,52]. In  
 263 addition, a second yaw control case (Y5) is constructed, for which a higher maximum yaw rate of  
 264  $\omega^{\max} = 5^\circ/\text{s}$  is selected. Although this significantly exceeds the capabilities of the abovementioned  
 265 turbine design concepts, this case will allow to assess whether significant gains in power could  
 266 be achieved by rapidly yawing turbine designs, such as low-inertia two-bladed teeter hinge wind  
 267 turbines [53].

268 Similar to earlier studies [13,36], also two induction control cases are considered, in which  
 269 turbines can adapt their thrust coefficient  $C'_T$  with a characteristic timescale  $\tau = 5 \text{ s}$ : an  
 270 underinductive case where turbines are restricted to lowering  $C'_T$  below the Betz-optimal value if  
 271 desired (I2, with  $C'_{T,\max} = 2$ ), and an overinductive case in which also higher  $C'_T$  values resulting  
 272 in increased thrust forces are allowed (I3, with  $C'_{T,\max} = 3$ ). Finally, for both the latter cases, also  
 273 the option of combining dynamic induction control with the yaw control of case Y is considered,  
 274 defining the yaw–induction cases I2Y and I3Y respectively. The cases investigated in this study are  
 275 summarized in Table 1.

## 276 4. Results & discussion

277 The current section presents and discusses the results of the optimal control cases. Firstly, the  
 278 convergence behavior is illustrated for a typical optimization window in Section 4.1, justifying the  
 279 optimization parameters discussed in previous section. Thereafter, Section 4.2 and 4.3 present the  
 280 results of the uniform and turbulent inflow cases respectively. Concluding, Section 4.4 compares both  
 281 simulation sets and identifies the most promising control approaches.

### 282 4.1. Convergence behavior

283 Figure 4 illustrates the convergence behavior within the second optimization window of the uniform  
 284 inflow case. Figure 4a shows that, although formal convergence is not achieved for any of the cases,  
 285 after 80 iterations, the relative ordering of the cases is clear and we assume that further improvements  
 286 in the cost function for an increased amount of iterations are marginal. From Figure 4b it can be  
 287 seen that the amount of PDE evaluations (forward or adjoint) is approximately twice the amount

**Table 1.** Setup parameters for optimal dynamic induction and yaw control cases

<b>Simulation parameters</b>			
Domain size	$L_x \times L_y \times H = 4.8 \times 2.4 \times 1 \text{ km}^3$		
Turbine dimensions	$D = 0.1H = 100 \text{ m}$		
Turbine spacing	$S_x = 6D, S_y = 6D$		
Windfarm layout	$N_t = 16 \text{ turbines} = 4 \text{ rows} \times 4 \text{ columns}$		
Grid size	$N_x \times N_y \times N_z = 256 \times 128 \times 128$		
Cell size	$\Delta_x \times \Delta_y \times \Delta_z = 18.75 \times 18.75 \times 7.8 \text{ m}^3$		
Time step	$\Delta t = 0.75 \text{ s}$		
<i>Uniform inflow</i>			
Hub height	$z_h/H = 0.5$		
Inflow velocity	$U_\infty = 8 \text{ m s}^{-1}$		
<i>Turbulent inflow</i>			
Hub height	$z_h/H = 0.1$		
Precursor pressure gradient	$\partial_x p_\infty = 2.5 \times 10^{-4} \text{ m s}^{-2}$		
Surface roughness	$z_0 = 10^{-4}H = 0.1 \text{ m}$		
<b>Optimization parameters</b>			
Optimization method	L-BFGS-B		
Hessian correction pairs	$m = 5$		
BFGS iterations	$N_{it} = 80 (\approx 160 \text{ PDE})$		
Optimization time window	$T = 300 \text{ s}$		
Flow advancement time window	$T_A = 150 \text{ s}$		
Total operation time	$T_{tot} = 900 \text{ s (6 windows)}$		
Cases		$C'_{T,\min}$	$C'_{T,\max}$
Reference	(R)	2	2
Yaw control	(Y)	2	2
Fast yaw control	(Y5)	2	2
Underinduction control	(I2)	<b>0</b>	2
Overinduction control	(I3)	<b>0</b>	<b>3</b>
Underinduction + yaw control	(I2Y)	<b>0</b>	2
Overinduction + yaw control	(I3Y)	<b>0</b>	<b>3</b>
			$\omega_{\max} [\text{°/s}]$

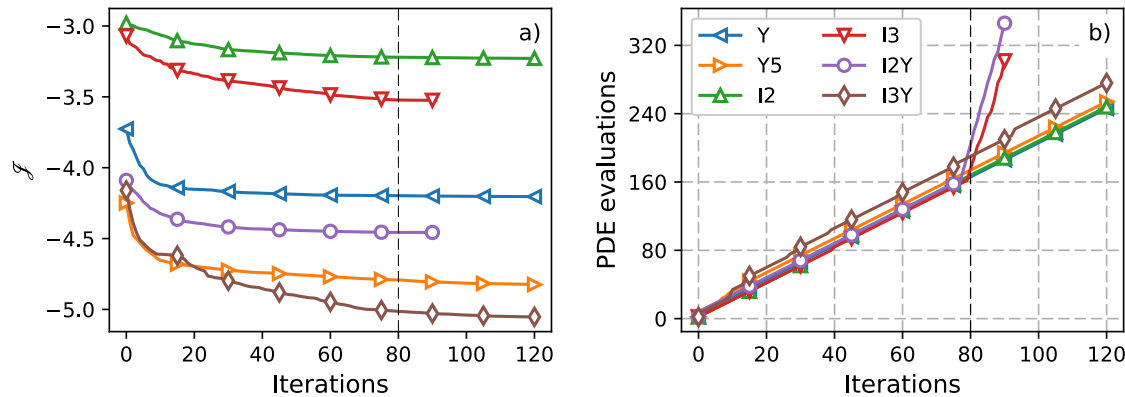


**Figure 4.** Convergence behavior for the second optimization window in uniform inflow. *a*) : Cost functional  $\mathcal{J}$ . *b*) : PDE evaluations (forward or adjoint). Markers represent every fifteenth iteration step.

288 of BFGS iterations, indicating that the optimizer mostly takes Newton steps without a further line  
289 search. The strong increase in PDE evaluations for I3 and I2Y can be explained by the fact that the  
290 limits of continuous adjoint gradient accuracy complicate satisfaction of the Wolfe conditions upon  
291 approaching a (local) optimum. Similar characteristics were observed for the turbulent case (not  
292 further shown here).

#### 293 4.2. Uniform inflow

294 Figure 5 depicts instantaneous planviews of velocity and vorticity at hub height at  $t = 450$  s for the  
295 reference case R, yawing case Y, overinductive case I3, and combined case I3Y. A first qualitative  
296 comparison between flow fields illustrates different mechanisms for increasing power extraction.  
297 Yawing case Y achieves wake direction, mixing, and later spreading through reorientation of turbine  
298 thrust forces. In contrast, overinductive case I3 increases mixing by periodically shedding vortex  
299 rings from upstream turbines, as indicated by the regions of increased vorticity in the turbine wakes.  
300 Similar behavior was identified from the analysis of prior induction control studies [54]. Combined  
301 yaw–induction case I3Y shows a superposition of the aforementioned behavior, i.e. redirected wakes  
302 with periodically shed vortices.

303 First, in §4.2.1 time-averaged power extraction and wind-farm efficiency are compared between  
304 cases. Second, in §4.2.2 yaw characteristics of the yaw-enabled control cases Y, Y5, I2Y, and I3Y are  
305 discussed. Time evolution of yaw angles is shown, and two distinct yawing regimes are identified.  
306 Finally, the induction characteristics of induction-enabled cases I2, I3, I2Y, and I3Y are shortly  
307 presented in §4.2.3.

#### 308 4.2.1. Power extraction and wind-farm efficiency

309 Figure 6 illustrates time-averaged wind-farm power results. Figure 6a shows the row-averaged  
310 power extraction of the optimal control and reference cases, normalized by first-row power in the  
311 reference case  $\bar{P}_{R1}^R$ . It is shown that all cases curtail first-row power by about 10 – 20% to the benefit  
312 of downstream rows. Furthermore, yaw-enabled cases Y, Y5, and I3Y achieve an almost flat power  
313 curve among rows, and significantly outperform the exclusively inductive cases I2 and I3, for which  
314 modest gains are obtained only in the second and third row. Note especially the last row of case I3Y,  
315 which achieves a power extraction close to freestream conditions.

316 Figure 6b depicts the wind farm efficiency, defined with respect to a situation in which all  
317 turbines extract the same power as a first-row reference case turbine, i.e.  $\eta_{farm} = \bar{P}_{farm}/(N_t \bar{P}_{R1}^R)$ . As

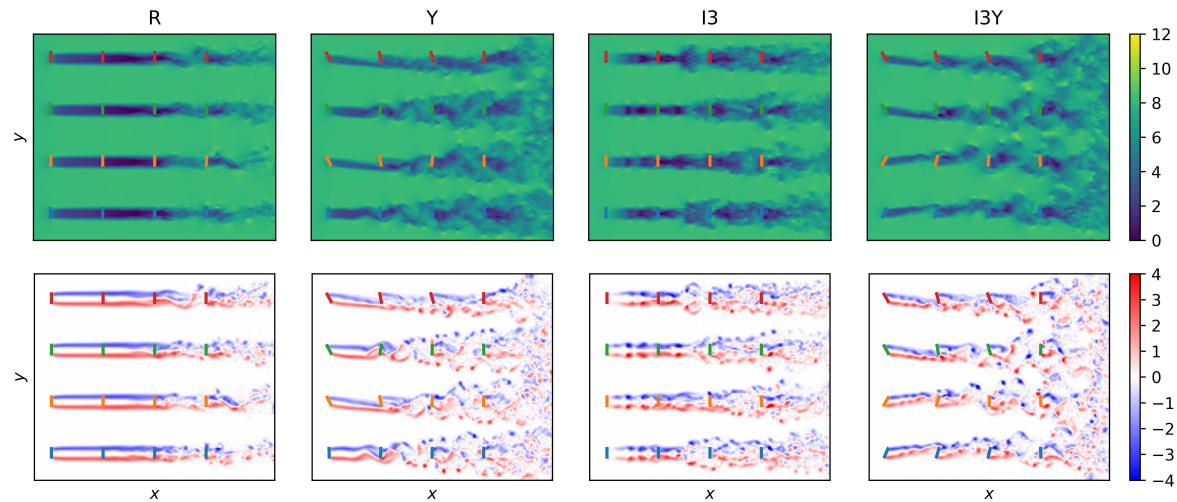


**Figure 5.** Instantaneous planviews at hub height for uniform inflow cases R, Y, I3, and I3Y at  $t = 450$  s. Top: Streamwise velocity. Coloring in  $\text{m s}^{-1}$ . Bottom: Wall-normal vorticity. Coloring in  $\text{s}^{-1}$ .

318 expected, the efficiency of the uncontrolled reference farm R is very low at around 40%. The inductive  
 319 cases I2 and I3 manage to increase the efficiency to approximately 50%, whereas the standard yawing  
 320 case Y attains an overall efficiency of about 77%. Further, it can be seen that, under uniform inflow  
 321 conditions, adding the possibility of fast yawing (case Y5) or underinduction (case I2Y) yields only  
 322 a very minor increase in wind-farm efficiency. In contrast, the combined overinductive yaw control  
 323 from case I3Y results in a significantly higher efficiency of about 84%, indicating the potential for  
 324 combining these control strategies under uniform inflow. The figure also includes results for two  
 325 additional control cases Ystat and YMndr that are based on simplified controls derived from the yaw  
 326 characteristics of the optimal control cases. These simplified control cases are further detailed and  
 327 discussed below.

#### 328 4.2.2. Yaw characteristics

329 Figure 7 illustrates the time evolution of normalized power extraction and yaw angle of the optimal  
 330 yawing cases (Y, Y5, I2Y, and I3Y), as defined in Table 1. The top panels of Figure 7 show that,  
 331 for all optimal yaw cases, power is curtailed to a limited extent in the first row, whereas power in  
 332 downstream rows is increased significantly after a delay corresponding to the wake advection time.

333 Turning to the time evolution of the yaw angle  $\theta$ , a first observation is that, although the four  
 334 columns of the considered wind farm are statistically equivalent in the reference case, their behavior  
 335 in an optimal control setting is heterogeneous. For example, for case Y, the first-row behavior of  
 336 the yaw angle  $\theta$  seems to exhibit a bifurcation between two limit cycles. On the one hand, the  
 337 first-row turbines in columns C1, C2, and C3 initially oscillate around the flow-aligned yaw angle  
 338 of  $0^\circ$ , triggering a *wake meandering* type of motion. Column C4 on the other hand directly turns to  
 339 a misaligned yaw angle of  $30^\circ$ , after which it shows some minor high frequency yaw oscillations.  
 340 As shown in panel Y of Figure 5, the former wake meandering mechanism mainly acts on increased  
 341 wake spreading in the lateral direction, and enhances recovery by increasing the contact area between  
 342 the wake and its surroundings. Turbine row 2 and 3 show more complex oscillations, with additional  
 343 variability in response to the unsteadiness in local flow conditions. In contrast, the first-row yaw  
 344 misalignment in column C4 creates a more shallow wake which is *redirected* such that it just misses  
 345 the downstream turbine. Downstream rows 2 and 3 exhibit some minor oscillations around a yaw  
 346 misalignment angle of  $\approx 17^\circ$ , causing further yaw redirection downstream. Since there is no further  
 347 downstream potential for wake mixing or redirection, the final row consistently shows a yaw angle  
 348 aligned with the mean flow. Similar time evolutions of the yaw angle are observed for column C2 of

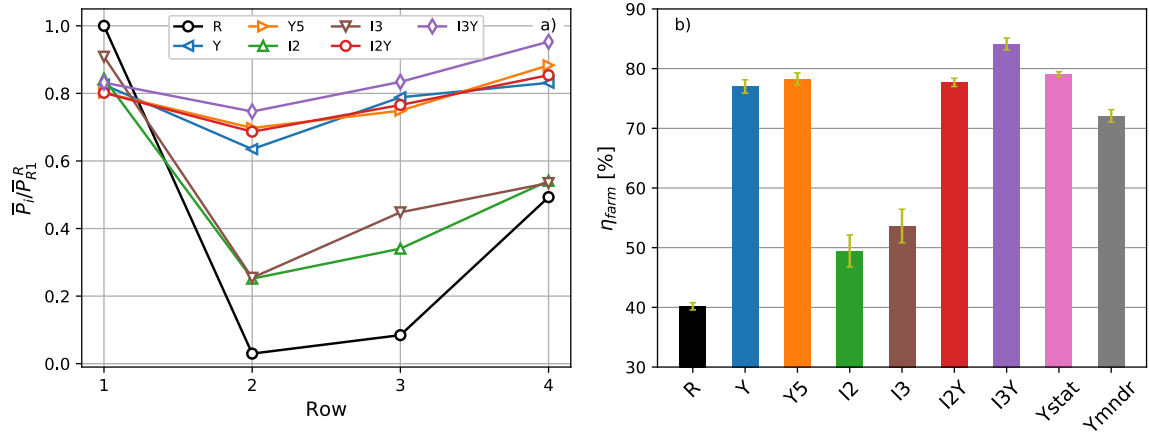


**Figure 6.** Wind-farm power extraction. *a)* Row-averaged power, normalized by first-row power of reference case R. *b)* Wind-farm efficiency  $\eta_{farm}$  compared to situation in which all turbines are first-row turbines of R case. Errorbars indicate confidence intervals of  $\pm 2$  standard deviations and are calculated using the procedure detailed in Appendix C of Ref. [14].

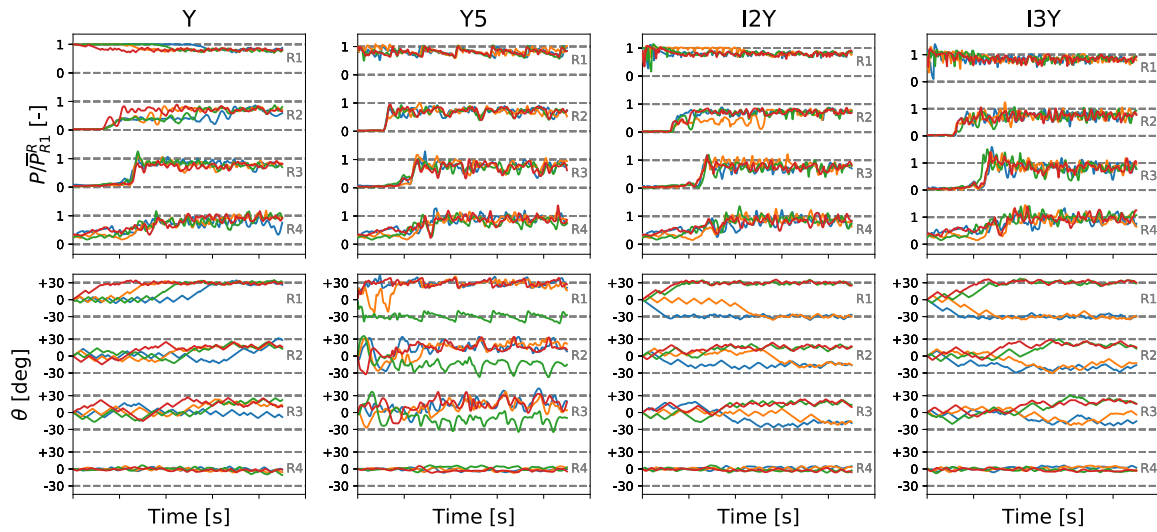


**Figure 7.** Time evolution of uniform inflow yaw-enabled cases. *Top:* Turbine power extraction  $P$ , normalized by mean first row power in the uncontrolled reference  $\bar{P}_{R1}^R$ . *Bottom:* Yaw angle  $\theta$ . Line colors indicate different turbine columns as indicated in Figure 3 (C1, C2, C3, C4), i.e. every line represents a single wind turbine.

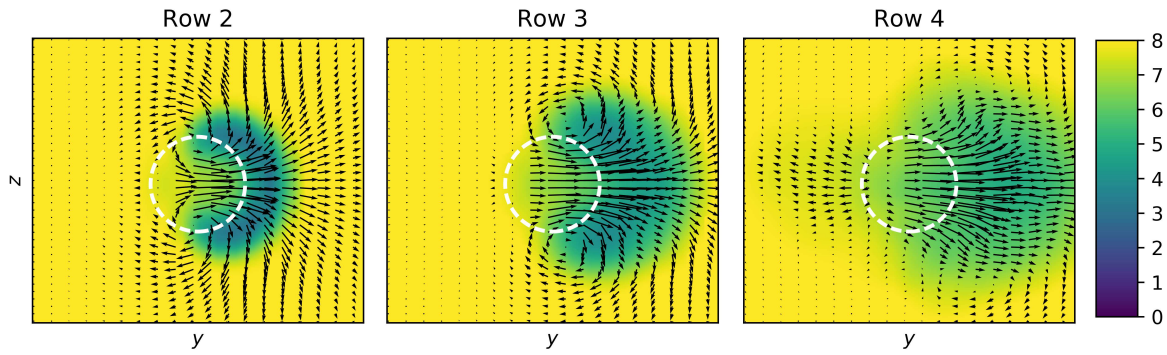


**Figure 8.** Time-averaged cross-sectional views of streamwise velocity  $\tilde{u}_x$  for case Y at a distance  $D/2$  upstream of the downstream turbines in column C4. Arrows represent the projection of the velocity vector on the cross-sectional plane. Dashed white lines indicate turbine rotor locations. Coloring in  $m s^{-1}$ .

349 the combined yaw-induction case I2Y. In cases I3Y and Y5, the wake meandering regime seems to be  
 350 virtually non-existent and wake redirection is dominant, except for the initial stage of the first-row  
 351 turbine in column C2. In summary, two distinct and relatively simple mechanisms for power increase  
 352 through yaw control are found: on the one hand a *dynamic* wake meandering regime is identified,  
 353 and on the other hand a *static* wake redirection regime is observed. These mechanisms are further  
 354 analyzed below.

### 355 Static yaw regime - wake redirection

356 Figure 8 shows cross sections of the time-averaged axial velocity field from case Y, taken at half a  
 357 rotor diameter upstream of rows 2, 3, and 4 in column C4, for which turbines directly go to static  
 358 yaw angles of  $30^\circ$ ,  $17^\circ$ , and  $17^\circ$  for the first, second, and third row respectively (see Figure 7). The  
 359 figure illustrates that the yaw misalignment of upstream turbines causes the wake to be redirected  
 360 away from the downstream ones. Moreover, as observed in recent studies, the wake induced by the  
 361 yaw-misaligned upstream turbines has a curled shape with counter-rotating vortices at its top and  
 362 bottom [22,24]. The current LES-based flow model allows to directly account for this in developing  
 363 the control strategies, as the wakes are curled just around the downstream turbines, resulting from a  
 364 trade-off between limiting upstream power loss and redirecting the wakes sufficiently. The static yaw  
 365 wake redirection regime observed in the optimal control simulations can be mimicked by imposing  
 366 fixed yaw misalignments corresponding to the aforementioned values. This simplified control case is  
 367 denoted as Ystat.

368 It can be seen from Figure 6b that Ystat yields approximately the same wind-farm efficiency  
 369 of 79% as the optimally controlled yawing cases Y and Y5, suggesting that, for the uniform inflow  
 370 case, any dynamic effects observed for turbines in the wake redirection regime are of very minor  
 371 importance. Furthermore, the fact that the expected value of Ystat is slightly higher than that of Y  
 372 and Y5 can be attributed to the fact that optimizations are not fully converged, finite-horizon effects  
 373 possibly have a small negative influence on the optimal control cases, and the wake meandering  
 374 regime that is present in some turbines for the optimal control cases yields slightly lower power than  
 375 the pure wake redirection of Ystat.

### 376 Dynamic yaw regime - wake meandering

377 Figure 9 shows row-averaged power spectra of the yaw angle  $\theta$ . We focus on relatively slow dynamics:  
 378 spectra are shown up to a Strouhal number  $St = fD/U_\infty = 0.8$ , corresponding to variations with a  
 379 time period longer than 15 s. The figure shows that, for the upstream rows 1 to 3, the variance of  
 380 the fast yawing case Y5 is significantly higher than the slow yawing cases Y, I2Y, and I3Y. The first

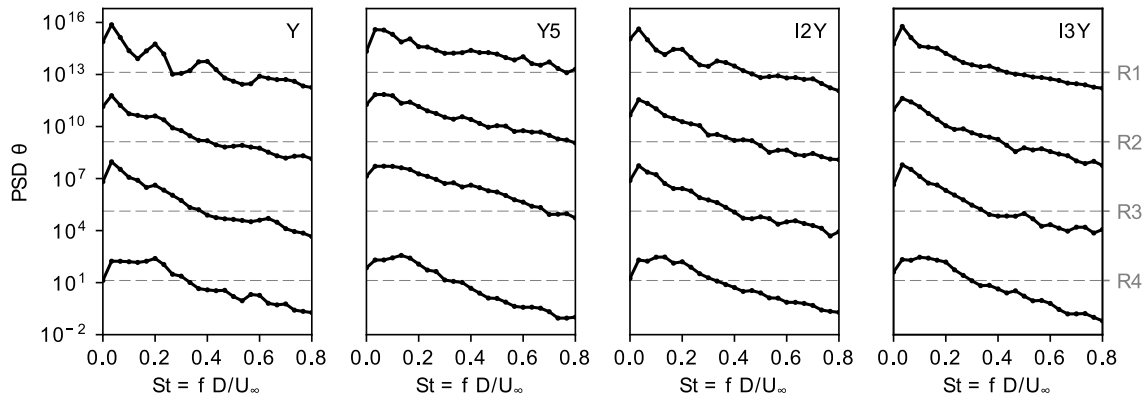


**Figure 9.** Row-averaged power spectral density estimate of yaw angle  $\theta$  as a function of Strouhal number  $St = fD/U_\infty$ . Spectra of different rows are shifted vertically for clarity. Horizontal dashed lines indicate identical reference values for each row.

row of case Y shows a significant peak around  $St = fD/U_\infty = 0.2$ , corresponding to the frequency of the aforementioned oscillations around aligned yaw angles, triggering wake meandering. Smaller subsequent peaks at harmonics of this frequency are also observed. Indeed, a Strouhal number in the range of 0.1 – 0.3 has been associated with natural wake meandering before in various studies [21,55]. Although attenuated, this peak seems to manifest itself to a limited degree in downstream rows as well. Furthermore, traces of this behavior are also observed for case I2Y, for which it was already mentioned that the first row of column C2 showed behavior consistent with a regime triggering wake meandering. In contrast, as observed qualitatively from Figure 7, cases Y5 and I3Y show no strongly coherent dynamic yaw characteristics, indicating that static wake redirection yaw is dominant here. Similar to the simplified static yaw case derived from the wake redirection behavior in previous paragraph, the wake meandering regime can be approximated by imposing a simple bang-bang control on the first row turbines, with an alternating yaw rate  $\omega = 0.3^\circ \text{ s}^{-1}$  in both directions with a frequency corresponding to a Strouhal number  $St = 0.2$ . The coherent dynamics and phase differences of the yaw rates in the downstream turbines are more complex. Therefore, these turbines are not yawed in the derived control case. This simplified case is further denoted as Ymndr. Figure 6b illustrated that, by simply applying this bang-bang control in the first-row turbine, a wind-farm efficiency of about 72% can be attained.

#### 4.2.3. Induction characteristics

Figure 10 illustrates the time evolution of normalized power extraction and thrust coefficient of the optimal induction cases (I2, I3, I2Y, and I3Y), as defined in Table 1. In contrast to the heterogeneous behavior in different columns for the yaw angles as shown in Figure 7 above, the induction coefficient behavior is similar for each column, and is illustrated for column C1 only. The top panels of Figure 10 indicate that, for the exclusively inductive cases I2 and I3, first-row power is pulsed severely, leading to intermittent increases in downstream power extraction. This differs from the combined yaw–induction cases, which show much smoother power extraction dynamics.

Also the thrust coefficient dynamics vary significantly between different cases: the first-row thrust coefficients of I2 and I3 exhibit periodic oscillatory traits, and the downstream rows of these cases show somewhat more chaotic dynamics in response to unsteady flow conditions resulting from upstream actuation. The period associated with the low-frequency components in the first-row thrust coefficient signal corresponds to the window length, i.e. 150 s, hence indicating that these cases are reacting to finite-horizon effects. The higher frequencies in this signal are associated with the shedding of vortex rings observed in Figure 11 as discussed above (see also Ref. [54]).

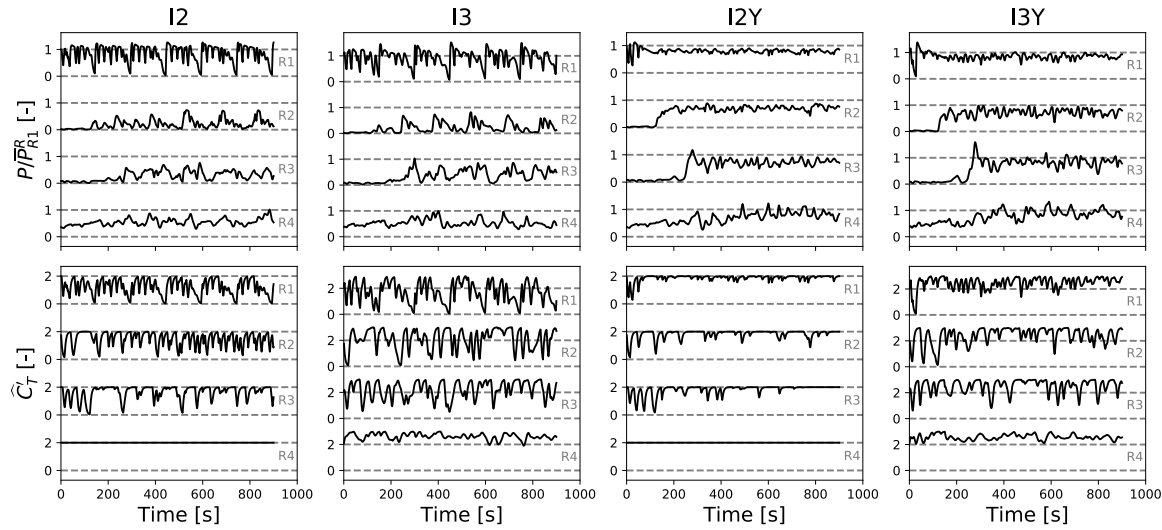


**Figure 10.** Time evolution of column C1 in uniform inflow induction-enabled cases. Top: Turbine power extraction  $P$ , normalized by mean first row power in the uncontrolled reference  $\bar{P}_{R1}^R$ . Bottom: Thrust coefficient  $\hat{C}_T'$ .

The underinductive yawing case I2Y features only minor deviations from the reference upper bound value of  $\hat{C}_T' = 2$ , especially for  $t > 200$  s. This can be explained based on the fact that, after this time, most turbines are yawed with respect to the incoming flow as shown in Figure 7, resulting in a lower axial velocity  $V$ , and hence a lower thrust force. Further reduction of this thrust force through lower thrust coefficients seems to show only very limited potential in increasing wind-farm power.

A converse reasoning can be used to explain the induction characteristics in case I3Y: the higher mean values of  $\hat{C}_T'$  in rows 1, 2, and 3 indicate that the wind farm benefits from compensating for the thrust force reduction in yawed turbines by increasing their axial induction. Note that, for the exclusively overinductive case I3, the mean thrust coefficient in the same rows is slightly lower than 2. The last-row turbines of both overinductive cases (I3 and I3Y) are both aligned with the mean flow and show a similar slight increase in the mean thrust coefficient.

The current section showed results for the steady uniform inflow cases. All controlled cases increase wind-farm efficiency by a significant amount, with the yaw-enabled cases significantly outperforming cases based on induction control only. Given the current quiescent ambient flow conditions, simple yaw behavior was identified, i.e. dynamic yaw triggering wake meandering on one hand, and steady yaw resulting in wake redirection on the other hand. Moreover, the simplified control cases Ystat and Ymndr derived from this behavior attain similar wind-farm efficiencies as the optimal control cases. In the next section, unsteady and turbulent inflow conditions are applied, and it is investigated whether similar simplified control methods can be applied.

#### 432 4.3. Turbulent inflow

433 Figure 11 illustrates snapshots of instantaneous streamwise velocity and wall-normal vorticity at hub  
 434 height at  $t = 450$  s for the reference case R, yawing case Y, overinductive case I3, and combined  
 435 yaw-overinductive case I3Y. In comparison to the uniform inflow set in Figure 5, the ambient  
 436 turbulence introduces background vorticity and already destabilizes turbine wakes even in the  
 437 reference case. Furthermore, wake behavior is much more chaotic and, although traces of wake  
 438 redirection can be observed for cases Y and I3Y, differences between the flow fields of different cases  
 439 are far less obvious than in uniform inflow.

440 Similar to the presentation of uniform inflow results in the previous section, firstly power  
 441 extraction and wind-farm efficiency are illustrated, after which the induction characteristics of

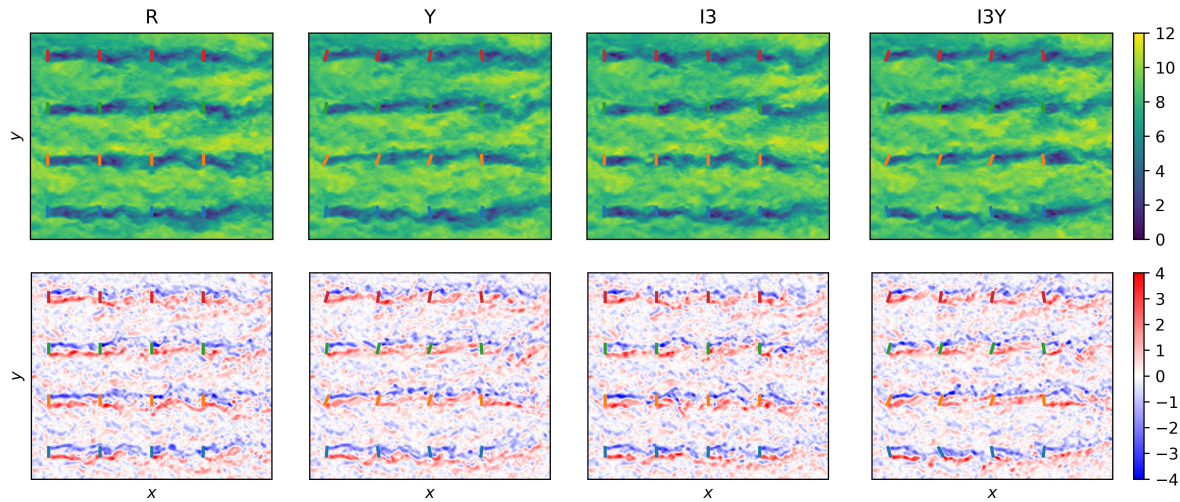


**Figure 11.** Instantaneous planviews at hub height for turbulent inflow cases at  $t = 450$  s. *Top:* Streamwise velocity. Coloring in  $\text{m s}^{-1}$ . *Bottom:* Wall-normal vorticity. Coloring in  $\text{s}^{-1}$ .

inductive cases are shown. Finally, the yaw and power characteristics of the yaw-enabled control cases are described.

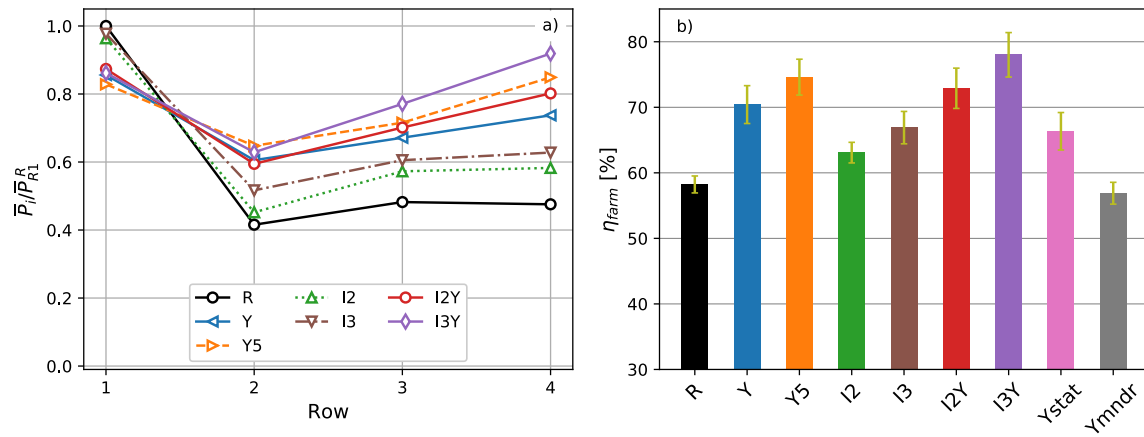
#### 4.3.1. Power extraction and wind-farm efficiency

Figure 12 depicts time-averaged wind-farm power results in the same manner as Figure 6. Figure 12a illustrates the row-averaged power extraction for the reference and optimal control cases. Note firstly the much higher power extraction in rows 2 and 3 for the reference case than in the uniform set, caused by the natural destabilization and mixing of turbine wakes by the ambient turbulence. Further, the figure shows that first-row power is being curtailed in all controlled cases. However, for the inductive cases I2 and I3, this curtailment is limited to below 5%. Significant power gains are achieved in all downstream rows of the inductive cases, except for the second row of I2. For the yaw-enabled cases, curtailment in the first row is smaller than in the uniform inflow set at around 15%, yet similar flattened power profiles are obtained.

Figure 12b illustrates the wind-farm efficiency for the reference case and the optimal control cases. Similar to the set of uniform inflow cases, also for turbulent inflow two simplified control cases Ystat and Ymndr are defined. These cases are further described and discussed below. A first observation is the higher reference efficiency at 58% compared to the uniform inflow value of 40%. Further, the power variability has increased in all cases, as indicated by the wider confidence intervals of the expected values (procedure for calculation of confidence intervals further detailed in Appendix C of Ref. [14]). The exclusively inductive cases I2 and I3 achieve wind-farm efficiencies of 63% and 67% respectively. The optimal yaw cases Y, Y5, I2Y, and I3Y attain slightly higher efficiencies of 70%, 75%, 73%, and 78% respectively. Note that, for unsteady ambient flow conditions, the faster yaw rate in case Y5 significantly increases the efficiency over the standard yaw case Y. The addition of underinduction control (I2Y) provides a small benefit over standard yaw control (Y), but the highest efficiency is again achieved by overinductive yaw control (I3Y).

#### 4.3.2. Yaw characteristics

Figure 13 indicates that both power and yaw angle exhibit significantly more variability compared to the uniform inflow set for all cases. Since wake meandering is already naturally triggered in turbulent boundary layers, the typical wake meandering regime with oscillations around yaw-aligned conditions is not directly observed for any of the cases here. The yaw-enabled cases all seem to turn to the wake redirection regime, characterized by approximately the same yaw angles



**Figure 12.** Wind-farm power extraction. a) Column-averaged power per row, normalized by first-row power of reference case R. b) Wind-farm efficiency  $\eta_{farm}$  compared to situation in which all turbines are first-row turbines of R case. Errorbars indicate confidence intervals of  $\pm 2$  standard deviations and are calculated using the procedure detailed in Appendix C of Ref. [14].

as in the uniform inflow cases. Note however that there is significant response of the yaw angle to background variability in local flow conditions for all cases, even causing the yaw angle to flip signs sometimes.

Figure 14 illustrates time-averaged cross sections of streamwise velocity  $D/2$  upstream of the column C4 turbines for reference case R and yawing case Y. Although wake redirection is complicated by the unsteady inflow, similar deflected and curl-shaped wakes with counter-rotating vortex pairs can be observed for case Y, albeit less explicit than in uniform inflow. Similar characteristics were observed for the other yawing cases Y5, I2Y, and I3Y (not further shown here). Given this information, a similar simplified steady yaw redirection case Ystat was defined, based on the same yaw angles as in the uniform inflow set, i.e.  $30^\circ$ ,  $17^\circ$ , and  $17^\circ$  in rows 1, 2, and 3 respectively. Figure 12b illustrates that, although steady yaw control successfully increases wind-farm efficiency to 66%, this value is surpassed significantly by the dynamic yawing cases presented above.

Figure 15 shows power spectral densities of the yaw angle  $\theta$ . Although much less apparent than in the uniform inflow, faint local increases in some of the spectra around  $St = 0.2$  can be seen. This raises the suspicion that also in the turbulent inflow case, for which wake meandering is already triggered naturally, the optimizer possibly reinforces meandering through yaw actuation in this frequency range. Therefore, an identical meandering case Ymnndr, with bang-bang yaw control at a rate of  $\omega = 0.3^\circ \text{ s}^{-1}$  in the first row was defined. However, Figure 12b indicates that this strategy does not lead to an increase in wind-farm efficiency.

#### 4.3.3. Induction characteristics

Figure 16 depicts the time evolution of power and induction coefficient for the inductive cases I2, I3, I2Y, and I3Y. Similar to the yaw angles described above, also the thrust coefficient appears much more chaotic than in the uniform inflow set, and shows no visually apparent signs of periodic repetitions in control signals. The underinductive cases I2 and I2Y show little deviation from the upper bound. The overinductive cases show similar behavior to the uniform inflow set, i.e. variations around the reference value of  $\hat{C}_T' = 2$  for I3, and a slight increase in mean thrust coefficient for I3Y.

#### 4.4. Discussion

Table 2 provides an overview of the efficiencies and power gains attained by each of the control cases described in the previous sections. From the table it can be seen that the relative order, based

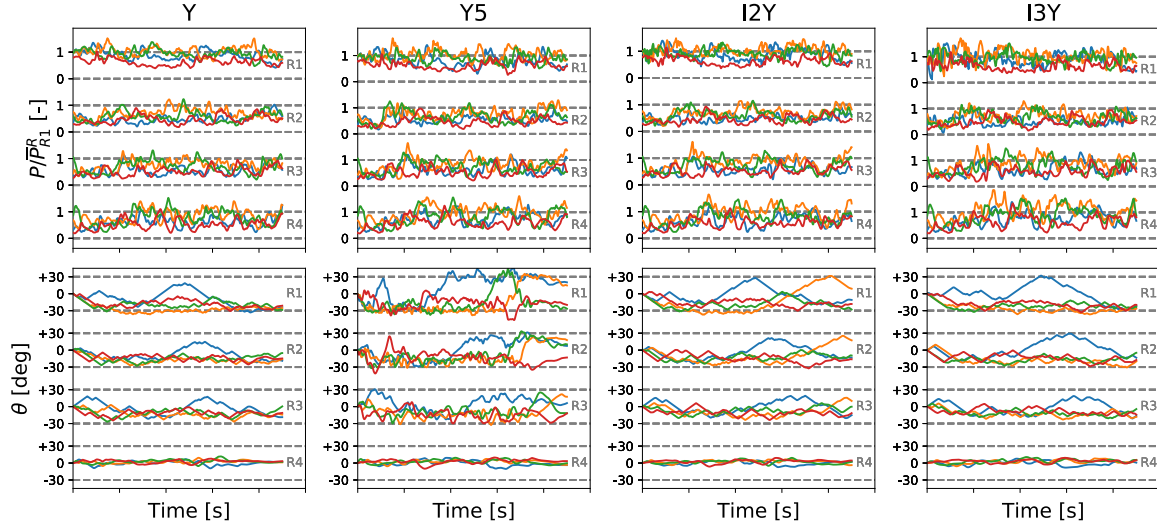


**Figure 13.** Time evolution of uniform inflow yaw-enabled cases. *Top:* Turbine power extraction  $P$ , normalized by mean first row power in the uncontrolled reference  $\bar{P}_{R1}^R$ . *Bottom:* Yaw angle  $\theta$ . Line colors indicate different turbine columns as indicated in Figure 3 (C1, C2, C3, C4), i.e. every line represents a single wind turbine.

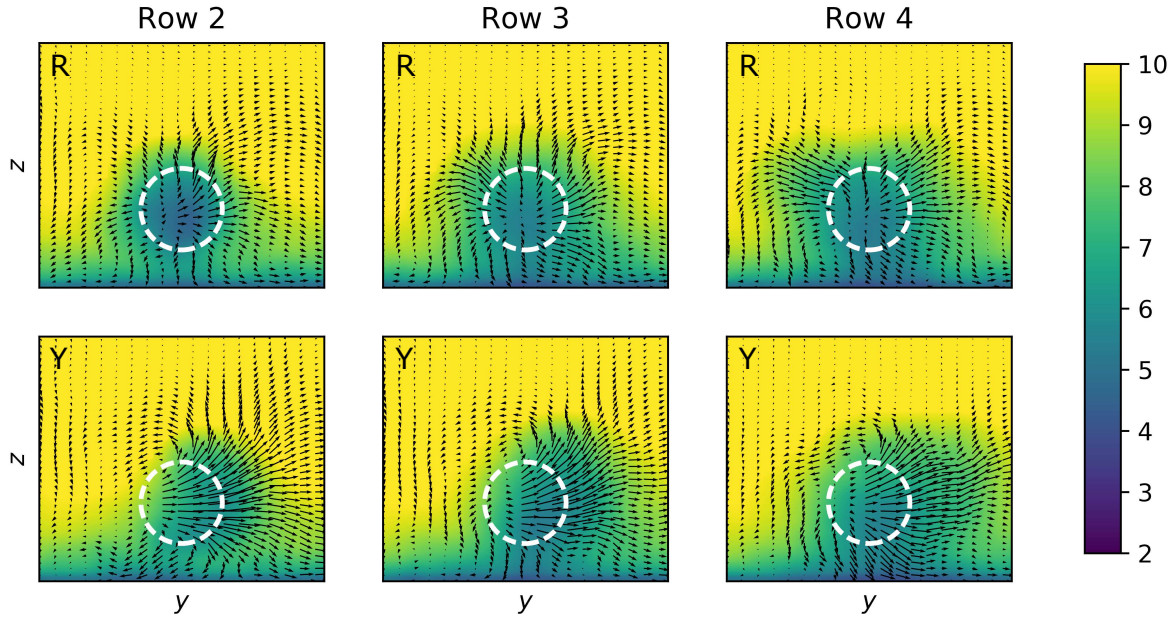


**Figure 14.** Time-averaged cross-sectional views of streamwise velocity  $\tilde{u}_x$  at a distance  $D/2$  upstream of the downstream turbines in column C4. Arrows represent the projection of the velocity vector on the cross-sectional plane. Dashed white lines indicate turbine rotor locations. Coloring in  $\text{m s}^{-1}$ .

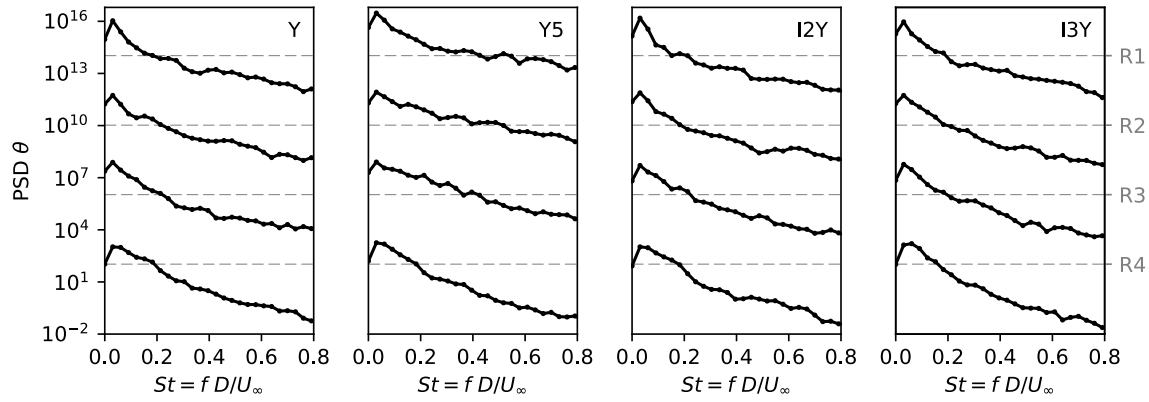


**Figure 15.** Row-averaged power spectral density estimate of yaw angle  $\theta$  as a function of Strouhal number  $St = fD/U_\infty$ . Spectra of different rows are shifted vertically for clarity. Horizontal dashed lines indicate identical reference values for each row.

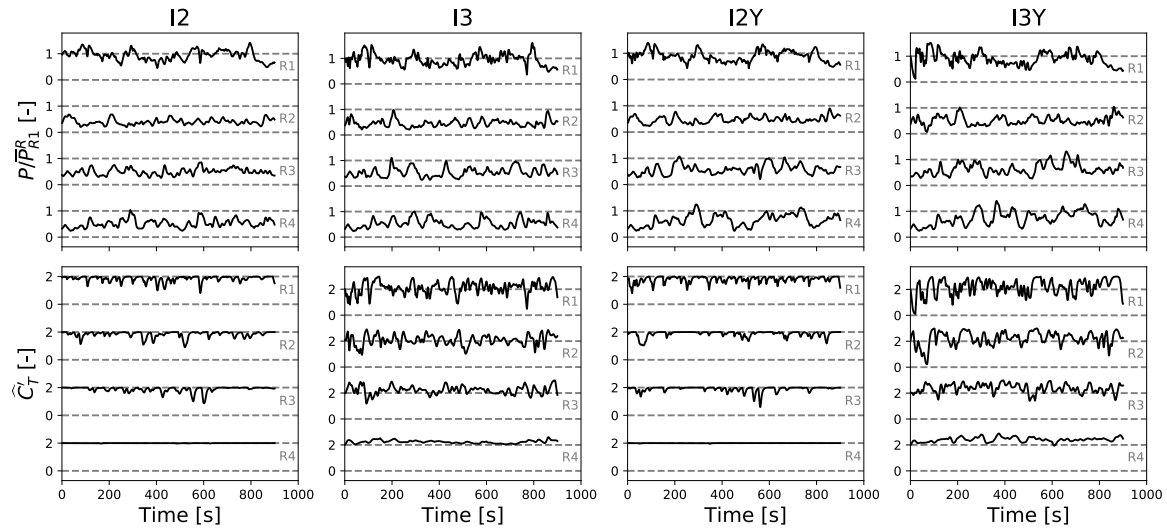


**Figure 16.** Time evolution of column C1 in uniform inflow induction-enabled cases. *Top:* Turbine power extraction  $P$ , normalized by mean first row power in the uncontrolled reference  $\bar{P}_{R1}^R$ . *Bottom:* Thrust coefficient  $\hat{C}_T'$ .

**Table 2.** Summary of wind-farm efficiencies and power gains. Optimal control cases are sorted based on farm efficiency.

			$\eta_{\text{farm}}^{\text{uniform}}$	$\eta_{\text{farm}}^{\text{turbulent}}$
<b>Greedy control</b>				
Reference	R		0.40	0.58
<b>Optimal control</b>				
Underinduction	I2		0.49 [+23%]	0.63 [+8%]
Overinduction	I3		0.53 [+34%]	0.67 [+15%]
Yaw	Y		0.77 [+92%]	0.70 [+21%]
Underinduction + yaw	I2Y		0.77 [+93%]	0.73 [+25%]
Fast yaw	Y5		0.78 [+95%]	0.75 [+28%]
Overinduction + yaw	I3Y		0.84 [+110%]	0.78 [+34%]
<b>Simplified control</b>				
Steady yaw	Ystat		0.79 [+97%]	0.66 [+14%]
Meandering yaw	Ymndr		0.72 [+79%]	0.57 [-2%]

501 on wind-farm efficiency, is the same for turbulent and uniform inflow conditions. For cases based  
 502 on exclusively induction control, i.e. I2 and I3, it can be seen that, although the *relative* increase is  
 503 larger for uniform inflow, the overall attainable wind-farm efficiency is higher for turbulent inflow  
 504 conditions.

505 Further results show that, for the current setup, all yaw-enabled cases consistently outperform  
 506 cases based solely on axial induction control. However, the gap between both is significantly larger  
 507 for uniform inflow than for turbulent inflow. The main reason for this is that the yawing cases  
 508 perform better in the absence of inflow turbulence due to the fact that a steady flow allows wakes  
 509 to be redirected more easily.

510 The benefits of combining underinductive axial induction control with yaw control (I2Y) are  
 511 relatively small: as shown in Figures 7 and 13, thrust coefficients are barely reduced from their initial  
 512 upper bound since the thrust forces exerted by turbines in yaw are already reduced through smaller  
 513 axial velocity components. In contrast, combining overinductive axial induction control with yaw  
 514 (I3Y) holds much greater promise: in addition to an increase in the mean thrust coefficients, also  
 515 dynamic thrust variations are observed in Figures 10 and 16, resulting in the highest wind-farm  
 516 efficiencies obtained for all cases. More specifically, for the current case, Table 2 shows that, given  
 517 turbulent inflow, the gains obtained by overinduction and yaw control are nearly additive, i.e. with  
 518 a 34% increase for the combined case I3Y, and increases of 21% and 15% for the yawing case Y and  
 519 overinductive case I3 respectively.

520 Based on the time evolution of yaw angles in Figures 7 and 13 two simplified cases were defined:  
 521 a static yaw control case (Ystat) that steadily deflects wakes away from downstream turbines, and  
 522 a dynamic yaw control case (Ymndr) that imposes an alternating bang-bang control in the first-row  
 523 turbine to reinforce downstream meandering of the wake. It is important to stress that these are  
 524 control strategies derived from observations in the optimal control simulations, but no optimization  
 525 was employed upon generating their control signals.

526 The yaw angles used in Ystat, as derived from the dynamic cases, are the same for uniform and  
 527 turbulent inflow. This indicates that the misalignment angles for steady yaw control are determined  
 528 by the wind-farm layout geometry, and the dependence on flow conditions is minor. Although Ystat  
 529 attains virtually identical efficiencies as the dynamic yaw cases Y and Y5 under uniform inflow,  
 530 its performance under unsteady turbulent flow conditions is surpassed significantly by the latter  
 531 dynamic cases. This suggests that, in turbulent flows, yaw dynamics play a significant role in  
 532 increasing wind-farm power in response to continuously changing flow conditions and incident flow

533 angles. This claim is supported by the observation that case Y5 significantly outperforms case Y for  
534 turbulent inflow, where this is not true for uniform inflow.

535 Further, simplified case Ymndr succeeds in significantly increasing wind-farm efficiency under  
536 uniform inflow, and even surpasses the optimization-based induction cases I2 and I3. This is a  
537 remarkable result for this very simple control strategy in which active turbines in the first row  
538 perform a simple flapping motion, whereas downstream turbines remain passive as in the reference  
539 case. However, in turbulent inflow conditions the same strategy did not lead to an increase in  
540 power extraction. This can be explained by the fact that meandering is already triggered naturally  
541 in turbulent boundary layers. Instead of actively reinforcing downstream wake meandering, the  
542 faint traces of spectral peaks at  $St = 0.2$  observed in Figure 15 might therefore simply be the  
543 response of yawing turbines to variability in the incident flow angle induced by natural upstream  
544 wake meandering. Another hypothesis is that reinforcing natural meandering requires more complex  
545 control of the yaw rate than the currently considered bang-bang control, and that the phase of yaw  
546 angle variations might have to be matched to local flow conditions. Further research is required to  
547 confirm or negate these hypotheses.

## 548 5. Summary

549 The current manuscripts investigated the potential of dynamic axial induction and dynamic yaw  
550 control for power maximization in an aligned  $4 \times 4$  wind farm using large-eddy simulations. A  
551 suite of control cases was defined: a set of axial induction control cases with underinductive and  
552 overinductive behavior, a set of yaw control cases with standard and high yaw rates, and a set of  
553 cases combining induction control with yaw control. For all control cases both uniform and turbulent  
554 inflow conditions were considered. In both inflow regimes, yaw control was found to be more  
555 effective than induction control for the given wind farm. Furthermore, the significant potential of  
556 combining overinduction control with yaw control was shown. Also, distinct regimes in the yaw  
557 control cases were identified, a steady yaw wake redirection regime, and a dynamic yawing regime  
558 reinforcing wake meandering. Although the former regime was found to be robust to the turbulence  
559 levels in the inflow, the latter only achieved an increase in power extraction for uniform conditions.  
560 For uniform inflow conditions, it was found that dynamic yawing adds little additional benefit  
561 over static wake redirection. In contrast, unsteady yawing allows turbines to adapt to continuously  
562 changing local flow conditions, and it was shown that this further increases farm power extraction  
563 for turbulent inflow conditions.

564 As discussed above, for the given wind-farm setup, yaw control is more favorable than induction  
565 control. An important remark to make is that, as e.g. observed in Figure 5 the yawing cases deflect  
566 wakes in the transversal direction, and extract energy from the unperturbed flow in the channels  
567 between turbine columns. However, in larger wind farms with greater streamwise extent, these  
568 channels are naturally depleted of kinetic energy in the downstream regions of the farm due to wake  
569 expansion (see for example Ref. [56], Figure 6). As a result, in the downstream regions of very large  
570 wind farms, power extraction is governed by vertical transport of kinetic energy [39,57]. Furthermore,  
571 transversal wake redirection in large yaw-controlled wind farms will lead to wakes interacting with  
572 other columns. In contrast, induction control allows for a more isotropic entrainment of kinetic energy,  
573 including in the vertical direction. The relative profitability of yaw and induction control is therefore  
574 probably dependent on wind-farm size, and turbines might prefer one mechanism over the other  
575 depending on their position within the farm. This is an interesting topic for future investigation.

576 Further, it is important to note that offshore wind farms typically operate at upstream turbulence  
577 intensity (TI) levels of 5–8%, in between the limit cases of uniform (TI = 0%) and turbulent inflow (TI  
578 = 8%) considered here [58,59]. Moreover, it was already mentioned that in stably stratified boundary  
579 layers, turbulence levels are further reduced and wake meandering is suppressed [49,50]. Therefore,  
580 the main differences between uniform and turbulent inflow observed here, i.e. the viability of the  
581 alternating yawing from Ymndr, and the importance of including dynamic yaw in addition to steady

582 redirection, should be further investigated based on a range of atmospheric conditions for particular  
 583 wind farms. Finally, note that the current study optimizes power at all costs, and did not account for  
 584 any undesirable loading characteristics. These should also be considered upon thoroughly comparing  
 585 induction and yaw control for practical purposes.

586 **Supplementary Materials:** The following are available online at [www.mdpi.com/link](http://www.mdpi.com/link), Figure S1: title, Table S1:  
 587 title, Video S1: title.

588 **Acknowledgments:** The authors acknowledge funding by the European Research Council (ActiveWindFarms,  
 589 grant no. 306471). The authors also acknowledge support from OPTEC (OPTimization in Engineering Center of  
 590 Excellence, KU Leuven), which is funded by the KU Leuven Research Council under grant no. PFV/10/002. The  
 591 computational resources and services in this work were provided by the VSC (Flemish Supercomputer Center),  
 592 funded by the Research Foundation Flanders (FWO) and the Flemish Government department EWI.

593 **Author Contributions:** WM and JM jointly set up the simulation studies in the current work. WM performed  
 594 code implementations and carried out the simulations. WM and JM jointly wrote the manuscript.

595 **Conflicts of Interest:** The authors declare no conflict of interest.

## 596 Appendix A. Derivation and verification of the adjoint yaw angle equation the adjoint gradient

597 In this appendix, we derive the adjoint yaw angle equation in Eq. 11 and the resulting adjoint cost  
 598 functional gradient in Eq. 13. Furthermore, the continuous adjoint gradient is verified through  
 599 comparison with a finite difference gradient approximation.

600 The derivation of the adjoint equations in this appendix is performed using the formal  
 601 Lagrangian approach [44,45], and is elaborated in a similar fashion as in Goit and Meyers [11]. Firstly,  
 602 inner products and functional gradients are defined in §A.1. Next, the Lagrangian functional for the  
 603 optimization problem at hand is introduced in §A.2. Then, the derivations of the adjoint gradient  
 604 expression and adjoint yaw angle equation are presented in §A.3 and §A.4 respectively. Finally, the  
 605 adjoint gradient is verified with a finite-difference gradient approximation in §A.5.

### 606 Appendix A.1. Definition of inner products and functional gradients

607 We define inner products between state variables  $\mathbf{q}_1$  and  $\mathbf{q}_2$ , and between control variables  $\boldsymbol{\varphi}_1$  and  $\boldsymbol{\varphi}_2$   
 608 respectively as

$$(q_1, q_2) = \int_0^T \int_{\Omega} \tilde{\mathbf{u}}_1 \cdot \tilde{\mathbf{u}}_2 \, dx \, dt + \int_0^T \int_{\Omega} \tilde{p}_1 \tilde{p}_2 \, dx \, dt + \int_0^T \tilde{\mathbf{C}}'_{T,1} \cdot \tilde{\mathbf{C}}'_{T,2} \, dt + \int_0^T \boldsymbol{\theta}_1 \cdot \boldsymbol{\theta}_2 \, dt, \quad (\text{A1})$$

$$(\boldsymbol{\varphi}_1, \boldsymbol{\varphi}_2) = \int_0^T \mathbf{C}'_{T,1} \cdot \mathbf{C}'_{T,2} \, dt + \int_0^T \boldsymbol{\omega}_1 \cdot \boldsymbol{\omega}_2 \, dt. \quad (\text{A2})$$

609 In these equations, the  $\cdot$  operator denotes a dot product between three-dimensional tensor fields, e.g.  
 610  $\tilde{\mathbf{u}}(\mathbf{x}, t) = [\tilde{u}_x(\mathbf{x}, t), \tilde{u}_y(\mathbf{x}, t), \tilde{u}_z(\mathbf{x}, t)]$ , or  $N_t$ -dimensional vectors, e.g.  $\boldsymbol{\theta}(t) = [\theta_1(t), \dots, \theta_{N_t}(t)]$ , where  
 611 appropriate. In addition, inner products between elements of state and control variables are defined  
 612 in a similar way, for instance

$$(\tilde{\mathbf{u}}_1, \tilde{\mathbf{u}}_2) = \int_0^T \int_{\Omega} \tilde{\mathbf{u}}_1 \cdot \tilde{\mathbf{u}}_2 \, dx \, dt, \quad \text{and} \quad (\boldsymbol{\omega}_1, \boldsymbol{\omega}_2) = \int_0^T \boldsymbol{\omega}_1 \cdot \boldsymbol{\omega}_2 \, dt. \quad (\text{A3})$$

613 The gradient of a differentiable functional is defined as the Riesz representation of its derivative [44,  
 614 45]. For example, using the definition of the Gâteaux derivative for a direction  $\delta\boldsymbol{\varphi}$  in a Hilbert space  
 615  $H$ , the gradient of the reduced cost functional  $\nabla \tilde{\mathcal{J}}$  is defined through

$$\tilde{\mathcal{J}}_{\boldsymbol{\varphi}}(\delta\boldsymbol{\varphi}) \equiv \frac{d}{d\alpha} \tilde{\mathcal{J}}(\boldsymbol{\varphi} + \alpha\delta\boldsymbol{\varphi}) \Big|_{\alpha=0} = (\nabla \tilde{\mathcal{J}}, \delta\boldsymbol{\varphi}) = \int_0^T \nabla \tilde{\mathcal{J}} \cdot \delta\boldsymbol{\varphi} \, dt \quad \forall \delta\boldsymbol{\varphi} \in H \quad (\text{A4})$$

**616** *Appendix A.2. Definition of Lagrangian functional*

**617** For ease of derivation and notation, we augment the original optimization problem in (1) with  
**618** some additional trivial state constraints containing the definitions for the geometric rotor footprint  
**619**  $\mathcal{R}_i$ , the rotor-perpendicular vector  $\mathbf{e}_{\perp,i}$ , and the rotor disk velocity  $V_i$ . The box constraints in (6) –  
**620** (7) are explicitly taken into account by the L–BFGS–B optimization algorithm, and are omitted in  
**621** the remainder of the derivation. The resulting augmented optimal control problem hence looks as  
**622** follows:<sup>1</sup>

$$\underset{\varphi, q}{\text{minimize}} \quad \mathcal{J}(\varphi, q) = - \int_0^T \sum_{i=1}^{N_t} \frac{1}{2} C'_{P,i} V_i^3 A_i dt \quad (\text{A5})$$

$$\text{s.t.} \quad \frac{\partial \tilde{\mathbf{u}}}{\partial t} + (\tilde{\mathbf{u}} \cdot \nabla) \tilde{\mathbf{u}} = -\nabla(\tilde{p} + \tilde{p}_\infty)/\rho - \nabla \cdot \boldsymbol{\tau}_{sgs} + \sum_{i=1}^{N_t} -\frac{1}{2} \hat{C}'_{T,i} V_i^2 \mathcal{R}_i(\mathbf{x}) \mathbf{e}_{\perp,i} \quad \text{in } \Omega \times (0, T], \quad (\text{A6})$$

$$\nabla \cdot \tilde{\mathbf{u}} = 0 \quad \text{in } \Omega \times (0, T], \quad (\text{A7})$$

$$\tau \frac{d\hat{C}'_{T,i}}{dt} = C'_{T,i} - \hat{C}'_{T,i} \quad i = 1 \dots N_t \text{ in } (0, T], \quad (\text{A8})$$

$$\frac{d\theta_i}{dt} = \omega_i \quad i = 1 \dots N_t \text{ in } (0, T], \quad (\text{A9})$$

$$\mathcal{R}_i(\mathbf{x}) = \int_{\Omega} G(\mathbf{s} - \mathbf{x}) H[D/2 - ||\mathbf{s} - \mathbf{t}_i||_2] \delta[(\mathbf{s} - \mathbf{t}_i) \cdot \mathbf{e}_{\perp,i}] d\mathbf{s} \quad i = 1 \dots N_t \text{ in } (0, T], \quad (\text{A10})$$

$$\mathbf{e}_{\perp,i} = \mathbf{e}_x \cos \theta_i + \mathbf{e}_y \sin \theta_i \quad i = 1 \dots N_t \text{ in } (0, T], \quad (\text{A11})$$

$$V_i = \frac{1}{A_i} \int_{\Omega} \mathcal{R}_i(\mathbf{s}) \tilde{\mathbf{u}} \cdot \mathbf{e}_{\perp,i} d\mathbf{s} \quad i = 1 \dots N_t \text{ in } (0, T]. \quad (\text{A12})$$

**623**

**624** Further, we define the Lagrangian of this optimization problem by adding the state constraints, with  
**625** shorthand notation  $\mathbf{B}(\varphi, q)$ , to the cost functional through inner product with the adjoint variables  
**626**  $q^* = [\xi, \pi, \sigma_1, \dots, \sigma_{N_t}, \eta_1, \dots, \eta_{N_t}]$ , which serve as Lagrange multipliers:

---

<sup>1</sup> Note that, throughout this text,  $\delta[a]$  denotes the Dirac delta function applied to a scalar argument  $a$ , whereas  $\delta h$  represents a variation of a functional  $h$ .

$$\begin{aligned}
\mathcal{L}(\boldsymbol{\varphi}, \boldsymbol{q}, \boldsymbol{q}^*) &\equiv \mathcal{J}(\boldsymbol{\varphi}, \boldsymbol{q}) + \left( \mathbf{B}(\boldsymbol{\varphi}, \boldsymbol{q}), \boldsymbol{q}^* \right) \\
&= \int_0^T \sum_{i=1}^{N_t} -\frac{1}{2} a \widehat{C}'_{T,i} V_i^3 A_i dt \\
&+ \int_0^T \int_{\Omega} \left\{ \frac{\partial \tilde{\mathbf{u}}}{\partial t} + (\tilde{\mathbf{u}} \cdot \nabla) \tilde{\mathbf{u}} + \nabla(\tilde{p} + \tilde{p}_{\infty})/\rho + \nabla \cdot \boldsymbol{\tau}_{sgs} - \sum_{i=1}^{N_t} \mathbf{f}_i \right\} \cdot \boldsymbol{\xi} dx dt \\
&+ \int_0^T \int_{\Omega} \left\{ \nabla \cdot \tilde{\mathbf{u}} \right\} \pi dx dt \\
&+ \int_0^T \sum_{i=1}^{N_t} \left\{ \tau \frac{d \widehat{C}'_{T,i}}{dt} - C'_{T,i} + \widehat{C}'_{T,i} \right\} \sigma_i dt \\
&+ \int_0^T \sum_{i=1}^{N_t} \left\{ \frac{d \theta_i}{dt} - \omega_i \right\} \eta_i dt \\
&+ \int_0^T \int_{\Omega} \sum_{i=1}^{N_t} \left\{ \mathcal{R}_i(\mathbf{x}) - \int_{\Omega} G(\mathbf{s} - \mathbf{x}) H[D/2 - ||\mathbf{s} - \mathbf{t}_i||_2] \delta[(\mathbf{s} - \mathbf{t}_i) \cdot \mathbf{e}_{\perp,i}] d\mathbf{s} \right\} \rho_i dx dt \\
&+ \int_0^T \sum_{i=1}^{N_t} \left\{ \mathbf{e}_{\perp,i} - \mathbf{e}_x \cos \theta_i - \mathbf{e}_y \sin \theta_i \right\} \cdot \gamma_i dt \\
&+ \int_0^T \sum_{i=1}^{N_t} \left\{ V_i - \frac{1}{A_i} \int_{\Omega} \mathcal{R}_i(\mathbf{s}) \tilde{\mathbf{u}} \cdot \mathbf{e}_{\perp,i} ds \right\} \chi_i dt. \tag{A13}
\end{aligned}$$

627 The adjoint equations in (8) – (11) can then be found by postulating vanishing gradients of the  
628 Lagrangian as  $\mathcal{L}_{q_j}(\delta q_j) = (\partial \mathcal{L} / \partial q_j, \delta q_j) = 0$  with respect to each of the state variables  $q_j$  in  
629  $\boldsymbol{q} = [\tilde{\mathbf{u}}, \tilde{p}, \widehat{C}'_{T,1}, \dots, \widehat{C}'_{T,N_t}, \theta_1, \dots, \theta_{N_t}]$  for all possible variations  $\delta q_j$  (see, e.g. Refs. [44,45,60]). Further,  
630 given that these equations are satisfied, the gradient of the reduced cost functional can be found  
631 by expressing the sensitivity of the Lagrangian to the control variables as  $\mathcal{L}_{\varphi_j}(\delta \varphi_j)$  for the control  
632 parameters  $\varphi_j$  in  $\boldsymbol{\varphi} = [C'_{T,1}, \dots, C'_{T,N_t}, \omega_1, \dots, \omega_{N_t}]$ . Since the reduced formulation of the optimization  
633 problem by definition implies that  $B(\boldsymbol{\varphi}, \boldsymbol{q}(\boldsymbol{\varphi})) = 0$ , it can be found that the reduced cost functional  $\tilde{\mathcal{J}}$   
634 and the Lagrangian  $\mathcal{L}$  are in fact equivalent [60], i.e.

$$\tilde{\mathcal{J}}(\boldsymbol{\varphi}) = \mathcal{L}(\boldsymbol{\varphi}, \boldsymbol{q}(\boldsymbol{\varphi}), \boldsymbol{q}^*) = \mathcal{J}(\boldsymbol{\varphi}, \boldsymbol{q}(\boldsymbol{\varphi})) + \left( \mathbf{B}(\boldsymbol{\varphi}, \boldsymbol{q}(\boldsymbol{\varphi})), \boldsymbol{q}^* \right) \tag{A14}$$

### 635 Appendix A.3. Derivation of adjoint gradient

636 The cost functional gradient  $\nabla \tilde{\mathcal{J}}$  can be found trivially by evaluating the derivative of the Lagrangian  
637 in (A13) with respect to the thrust setpoints and yaw rate controls as

$$\mathcal{L}_{C'_{T,i}}(\delta C'_{T,i}) = (\partial \mathcal{L} / \partial C'_{T,i}, \delta C'_{T,i}) = (\partial \tilde{\mathcal{J}} / \partial \widehat{C}'_{T,i}, \delta \widehat{C}'_{T,i}) = \int_0^T -\sigma_i \delta C'_{T,i} dt, \tag{A15}$$

$$\mathcal{L}_{\omega_i}(\delta \omega_i) = (\partial \mathcal{L} / \partial \omega_i, \delta \omega_i) = (\partial \tilde{\mathcal{J}} / \partial \omega_i, \delta \omega_i) = \int_0^T -\eta_i \delta \omega_i dt. \tag{A16}$$

638 Hence leading to the gradient expression given in (13):

$$\nabla \tilde{\mathcal{J}} \equiv \begin{bmatrix} \partial \tilde{\mathcal{J}} / \partial C'_T \\ \partial \tilde{\mathcal{J}} / \partial \omega \end{bmatrix} = \begin{bmatrix} -\sigma \\ -\eta \end{bmatrix}. \tag{A17}$$

**639** Appendix A.4. Derivation of adjoint yaw angle equation

**640** The current section discusses the derivation of the adjoint yaw angle Equation (11). To keep notations  
**641** concise and the derivation clear, we will proceed by first deriving some auxiliary adjoint equations for  
**642** the rotor footprint  $\mathcal{R}_i$  and the disk velocity  $V_i$ . These will yield straightforward algebraic expressions  
**643** for the adjoint variables  $\rho_i$  and  $\chi_i$  respectively, which will be substituted within the derivation of the  
**644** equation for the adjoint rotor-perpendicular vector  $\gamma_i$ . Thereafter, the adjoint yaw angle equation for  
**645** the adjoint variable  $\eta_i$  will follow in a straightforward manner.

**646** Appendix A.4.1. Adjoint disk velocity equation

**647** The adjoint disk velocity equation for the adjoint variable  $\chi_i$  is found by expressing the functional  
**648** derivative of the Lagrangian  $\mathcal{L}$  to the disk velocity  $V_i$ , and equalizing to zero for all possible  
**649** variations  $\delta V_i$ , with  $i = 1 \dots N_t$ :

$$\mathcal{L}_{V_i}(\delta V_i) = (\partial \mathcal{L} / \partial V_i, \delta V_i) = \int_0^T -\frac{1}{2} a \hat{C}'_{T,i} 3 V_i^2 A_i \delta V_i dt + \int_0^T \frac{1}{2} \hat{C}'_{T,i} 2 V_i X_i A_i \delta V_i dt + \int_0^T \chi_i \delta V_i dt = 0. \quad (A18)$$

**650** This leads to the following expression for the adjoint variable  $\chi_i$ :

$$\chi_i = \frac{1}{2} \hat{C}'_{T,i} V_i (3aV_i - 2X_i) A_i \quad \text{for } i = 1 \dots N_t. \quad (A19)$$

**651** Appendix A.4.2. Adjoint rotor footprint equation

**652** The adjoint rotor footprint equation for the adjoint variable  $\rho_i$  is found by expressing the derivative  
**653** of the Lagrangian  $\mathcal{L}$  to the footprint  $\mathcal{R}_i$ :

$$\mathcal{L}_{\mathcal{R}_i}(\delta \mathcal{R}_i) = \int_0^T \int_{\Omega} \frac{1}{2} \hat{C}'_{T,i} V_i^2 \mathbf{e}_{\perp,i} \cdot \boldsymbol{\xi} \delta \mathcal{R}_i dx dt + \int_0^T \int_{\Omega} \rho_i \delta \mathcal{R}_i dx dt + \int_0^T \int_{\Omega} -\frac{\chi_i}{A_i} \tilde{\mathbf{u}} \cdot \mathbf{e}_{\perp,i} \delta \mathcal{R}_i dx dt = 0, \quad (A20)$$

**654** leading to a straightforward expression of the adjoint variable  $\rho_i$ :

$$\rho_i = \left( \frac{\chi_i}{A_i} \tilde{\mathbf{u}} - \frac{1}{2} \hat{C}'_{T,i} V_i^2 \boldsymbol{\xi} \right) \cdot \mathbf{e}_{\perp,i} = \frac{1}{2} \hat{C}'_{T,i} V_i \left( 3aV_i \tilde{\mathbf{u}} - 2X_i \tilde{\mathbf{u}} - V_i \boldsymbol{\xi} \right) \cdot \mathbf{e}_{\perp,i} \quad \text{for } i = 1 \dots N_t. \quad (A21)$$

**655** Appendix A.4.3. Adjoint rotor-perpendicular vector equation

**656** Similar to the previous sections, the equation for the adjoint rotor-perpendicular vector  $\gamma_i$  is derived  
**657** by expressing the derivative of the Lagrangian  $\mathcal{L}$  to  $\mathbf{e}_{\perp,i}$ :

$$\begin{aligned} \mathcal{L}_{\mathbf{e}_{\perp,i}}(\delta \mathbf{e}_{\perp,i}) &= \int_0^T \int_{\Omega} \frac{1}{2} \hat{C}'_{T,i} V_i^2 \mathcal{R}_i \boldsymbol{\xi} \cdot \delta \mathbf{e}_{\perp,i} dx dt - \int_0^T \int_{\Omega} \frac{\chi_i}{A_i} \mathcal{R}_i \tilde{\mathbf{u}} \cdot \delta \mathbf{e}_{\perp,i} dx dt + \int_0^T \gamma_i \cdot \delta \mathbf{e}_{\perp,i} dt \\ &\quad + \int_0^T \int_{\Omega} -\rho_i \left\{ \int_{\Omega} G(s-x) H[D/2 - \|s-t_i\|_2] \delta'[(s-t_i) \cdot \mathbf{e}_{\perp,i}] (s-t_i) \cdot \delta \mathbf{e}_{\perp,i} ds \right\} dx dt. \end{aligned} \quad (A22)$$

**658** The final term in the equation above requires some further attention. The derivative operator on  
**659** the Dirac delta function can be transferred to the other terms using partial integration by invoking  
**660** a coordinate transformation from the LES reference frame ( $e_x, e_y, e_z$ ) to the rotor reference frame

<sup>661</sup> ( $e_{\perp,i}, e_{\parallel,i}, e_z$ ), defining a new integration variable  $\zeta = R\mathbf{s}$  with  $R$  a rotation matrix from the LES to the  
<sup>662</sup> rotor reference. In doing so, the term between brackets in Equation (A22) can be rewritten as

$$\begin{aligned} & \int_{\Omega} G(\mathbf{s} - \mathbf{x}) H[D/2 - ||\mathbf{s} - \mathbf{t}_i||_2] \frac{d\delta[(\mathbf{s} - \mathbf{t}_i) \cdot e_{\perp,i}]}{d(\mathbf{s} - \mathbf{t}_i) \cdot e_{\perp,i}} (\mathbf{s} - \mathbf{t}_i) d\mathbf{s} \\ &= \int_{\Omega} G(\zeta - R\mathbf{x}) H[D/2 - ||\zeta - R\mathbf{t}_i||_2] \frac{d\delta[(\zeta_1 - R\mathbf{t}_i) \cdot \hat{\zeta}_1]}{d\zeta_1} (\zeta - R\mathbf{t}_i) d\zeta \\ &= - \int_{\Omega} \frac{d}{d\zeta_1} \left\{ G(\zeta - R\mathbf{x}) H[D/2 - ||\zeta - R\mathbf{t}_i||_2] (\zeta - R\mathbf{t}_i) \right\} \delta[(\zeta_1 - (R\mathbf{t}_i)_1)] d\zeta, \end{aligned} \quad (\text{A23})$$

<sup>663</sup> where the boundary terms drop out by the definition of the Dirac delta function. Furthermore, using  
<sup>664</sup> the chain rule and properties of the Dirac delta function the expression above can be written as

$$\begin{aligned} & - \int_{\Omega} \frac{d}{d\zeta_1} \left\{ G(\zeta - R\mathbf{x}) H[D/2 - ||\zeta - R\mathbf{t}_i||_2] (\zeta - R\mathbf{t}_i) \right\} \delta[(\zeta_1 - (R\mathbf{t}_i)_1)] d\zeta \\ &= - \int_{\Omega} G(\zeta - R\mathbf{x}) H[D/2 - ||\zeta - R\mathbf{t}_i||_2] \delta[(\zeta_1 - (R\mathbf{t}_i)_1)] \left\{ \hat{\zeta}_1 - \frac{12\zeta_1 - (R\mathbf{x})_1}{\Delta^2} (\zeta - R\mathbf{t}_i) \right\} d\zeta \\ &= - \int_{\Omega} G(\mathbf{s} - \mathbf{x}) H[D/2 - ||\mathbf{s} - \mathbf{t}_i||_2] \delta[(\mathbf{s} - \mathbf{t}) \cdot e_{\perp,i}] \left\{ e_{\perp,i} - \frac{12(\mathbf{s} - \mathbf{x}) \cdot e_{\perp,i}}{\Delta^2} (\mathbf{s} - \mathbf{t}_i) \right\} d\mathbf{s}. \end{aligned} \quad (\text{A24})$$

<sup>665</sup> Where the last step transforms the coordinate system back to the LES frame of reference. Further,  
<sup>666</sup> defining the auxiliary variable  $Q_i = \int_{\Omega} \frac{12(\mathbf{s} - \mathbf{x}) \cdot e_{\perp,i}}{\Delta^2} (\mathbf{s} - \mathbf{t}_i) G(\mathbf{s} - \mathbf{x}) H[D/2 - ||\mathbf{s} - \mathbf{t}_i||_2] \delta[(\mathbf{s} - \mathbf{t}) \cdot e_{\perp,i}] d\mathbf{s}$  for ease of notation, we find

$$\int_{\Omega} G(\mathbf{s} - \mathbf{x}) H[D/2 - ||\mathbf{s} - \mathbf{t}_i||_2] \delta'[(\mathbf{s} - \mathbf{t}_i) \cdot e_{\perp,i}] (\mathbf{s} - \mathbf{t}_i) d\mathbf{s} = -\mathcal{R}_i e_{\perp,i} + Q_i. \quad (\text{A25})$$

<sup>668</sup> Substituting expression (A25) into Equation (A22), along with the expressions for  $\rho_i$  (Equation A21)  
<sup>669</sup> and  $\chi_i$  (Equation A19) yields:

$$\begin{aligned} \mathcal{L}_{e_{\perp,i}}(\delta e_{\perp,i}) &= - \int_0^T \int_{\Omega} \frac{1}{2} \widehat{C}'_{T,i} V_i \left\{ 3aV_i \tilde{\mathbf{u}} - 2X_i \tilde{\mathbf{u}} - V_i \xi \right\} \mathcal{R}_i \cdot \delta e_{\perp,i} dx dt + \int_0^T \gamma_i \cdot \delta e_{\perp,i} dt \\ &+ \int_0^T \int_{\Omega} \frac{1}{2} \widehat{C}'_{T,i} V_i \left\{ (3aV_i \tilde{\mathbf{u}} - 2X_i \tilde{\mathbf{u}} - V_i \xi) \cdot e_{\perp,i} \right\} \mathcal{R}_i e_{\perp,i} \cdot \delta e_{\perp,i} ds \\ &- \int_0^T \int_{\Omega} \frac{1}{2} \widehat{C}'_{T,i} V_i \left\{ (3aV_i \tilde{\mathbf{u}} - 2X_i \tilde{\mathbf{u}} - V_i \xi) \cdot e_{\perp,i} \right\} Q_i \cdot \delta e_{\perp,i} ds. \end{aligned} \quad (\text{A26})$$

<sup>670</sup> Since there is no rotor tilt, it can be seen that  $\mathbf{v} - (\mathbf{v} \cdot e_{\perp,i}) e_{\perp,i} = (\mathbf{v} \cdot e_{\parallel,i}) e_{\parallel,i}$ , for any vector  $\mathbf{v}$  in  
<sup>671</sup>  $\Omega \times (0, T]$ . Hence,

$$\begin{aligned} \mathcal{L}_{e_{\perp,i}}(\delta e_{\perp,i}) &= \int_0^T \gamma_i \cdot \delta e_{\perp,i} dt \\ &- \int_0^T \int_{\Omega} \frac{1}{2} \widehat{C}'_{T,i} V_i \left\{ (3aV_i \tilde{\mathbf{u}} - 2X_i \tilde{\mathbf{u}} - V_i \xi) \cdot e_{\parallel,i} \right\} \mathcal{R}_i e_{\parallel,i} \cdot \delta e_{\perp,i} dx dt \\ &- \int_0^T \int_{\Omega} \frac{1}{2} \widehat{C}'_{T,i} V_i \left\{ (3aV_i \tilde{\mathbf{u}} - 2X_i \tilde{\mathbf{u}} - V_i \xi) \cdot e_{\perp,i} \right\} Q_i \cdot \delta e_{\perp,i} ds \end{aligned} \quad (\text{A27})$$

<sup>672</sup> Equating to zero finally yields the expression for the adjoint rotor-perpendicular vector  $\gamma_i$ :

$$\gamma_i = \frac{1}{2} \widehat{C}'_{T,i} V_i \int_{\Omega} \left[ \left\{ \left( 3aV_i \tilde{\mathbf{u}} - 2X_i \tilde{\mathbf{u}} - V_i \xi \right) \cdot \mathbf{e}_{\parallel,i} \right\} \mathcal{R}_i \mathbf{e}_{\parallel,i} + \left\{ \left( 3aV_i \tilde{\mathbf{u}} - 2X_i \tilde{\mathbf{u}} - V_i \xi \right) \cdot \mathbf{e}_{\perp,i} \right\} \mathbf{Q}_i \right] ds. \quad (\text{A28})$$

**673 Appendix A.4.4. Adjoint yaw angle equation**

**674** The current section derives the adjoint equation for the adjoint yaw angle  $\eta_i$ , required for the  
**675** evaluation of the cost functional yaw sensitivity in Equation (A16). Similar to previous sections, the  
**676** derivation starts by expressing the functional derivative of the Lagrangian to the yaw angle  $\theta_i$ :

$$\mathcal{L}_{\theta_i}(\delta\theta_i) = \int_0^T \gamma_i \cdot \left\{ \mathbf{e}_x \sin \theta_i - \mathbf{e}_y \cos \theta_i \right\} \delta\theta_i dt + \int_0^T \frac{d\delta\theta_i}{dt} \eta_i dt \quad (\text{A29})$$

$$= \int_0^T \left\{ -\frac{d\eta_i}{dt} - \mathbf{e}_{\parallel,i} \cdot \gamma_i \right\} \delta\theta_i dt = 0, \quad (\text{A30})$$

**677** Where partial integration on the time derivative is performed, and a terminal condition  $\eta_i(T) = 0$  is  
**678** applied, leading to vanishing boundary terms. This yields an ODE for  $\eta_i$ :

$$-\frac{d\eta_i}{dt} = \mathbf{e}_{\parallel,i} \cdot \gamma_i \quad \text{for } i = 1 \dots N_t. \quad (\text{A31})$$

**679** Substituting the expression for  $\gamma_i$  from Equation (A28), this expression can be rewritten as

$$-\frac{d\eta_i}{dt} = \frac{1}{2} \widehat{C}'_{T,i} V_i \int_{\Omega} \left[ \left\{ \left( 3aV_i \tilde{\mathbf{u}} - 2X_i \tilde{\mathbf{u}} - V_i \xi \right) \cdot \mathbf{e}_{\parallel,i} \right\} \mathcal{R}_i + \left\{ \left( 3aV_i \tilde{\mathbf{u}} - 2X_i \tilde{\mathbf{u}} - V_i \xi \right) \cdot \mathbf{e}_{\perp,i} \right\} \mathcal{Q}_i \right] ds, \quad (\text{A32})$$

**680** which is the adjoint equation for  $\eta_i$  featured in Equation (11). In this equation, the shorthand notation  
**681** for the filter kernel  $\mathcal{Q}_i$  is introduced as:

$$\mathcal{Q}_i = \mathbf{Q}_i \cdot \mathbf{e}_{\parallel,i} = \int_{\Omega} \frac{12(s-x) \cdot \mathbf{e}_{\perp,i}}{\Delta^2} G(s-x) H[D/2 - \|s-t_i\|_2] \delta[(s-t) \cdot \mathbf{e}_{\perp,i}] (s-t_i) \cdot \mathbf{e}_{\parallel,i} ds. \quad (\text{A33})$$

**682** Figure A1 illustrates both the original filter kernel  $\mathcal{R}$  and the new filter kernel  $\mathcal{Q}_i$ . It can be seen from  
**683** the figure that  $\mathcal{Q}_i$  quantifies the rate of change in the rotor geometrical footprint  $\mathcal{R}_i$  upon perturbing  
**684** the yaw angle  $\theta$ . Therefore,  $\mathcal{Q}_i$  can be regarded as a yaw-sensitivity footprint. Further, given Equation  
**685** (A16), it can be seen that the right-hand-side of Equation (A32) acts as a driving term for the yaw  
**686** rate sensitivity. The first term in the right-hand-side is associated with the flow currently parallel  
**687** to the rotor, which is hence not captured given its current orientation, imposing an incentive for  
**688** reorientation of the rotor. The second on the other hand is associated with the flow perpendicular  
**689** to the rotor just before or behind the rotor plane. This term causes an incentive for yawing since a  
**690** change in rotor locus (i.e. where the flow field is sampled by the ADM) would allow power to be  
**691** extracted from these terms.

**692 Appendix A.5. Verification of adjoint gradient**

**693** The current section aims to verify the continuous adjoint method applied in this manuscript through  
**694** comparison with a finite-difference approximation of the cost functional gradient. Since the accuracy  
**695** of the continuous adjoint method is dependent on the spatiotemporal resolution with which the  
**696** equations are discretized, the test is performed on a case with identical resolution as the cases defined

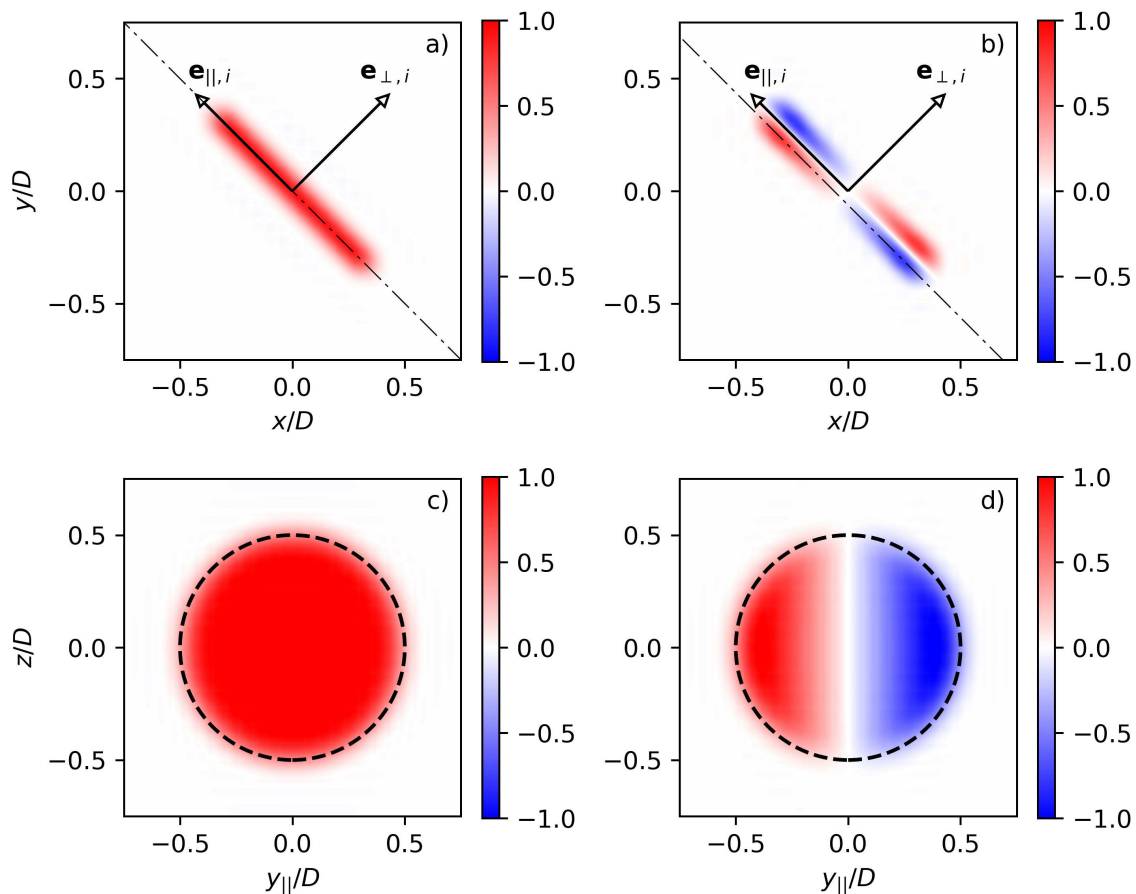


**Figure A1.** Geometrical filter kernels in Equation (A32). *a,c*) Original stationary rotor footprint  $\mathcal{R}$ . *b,d*) New yaw-sensitivity footprint  $\mathcal{Q}$ . *a,b*) Planview at hub height. *c,d*) Cross section through plane indicated by dot dashed line in *a,b*.

in the main text. To limit computational cost, a domain of reduced size with only 2 aligned turbines is considered. The simulation domain of  $2.4 \times 0.6 \times 0.5 \text{ km}^3$  is discretized on a grid of  $128 \times 32 \times 64$ , resulting in a grid resolution of  $18.75 \times 18.75 \times 7.8 \text{ m}^3$  simulated over a time horizon of 300 s with time steps of 0.75 s, identical to the simulations in the main text (see Table 1).

The finite difference method approximates the Gâteaux derivative in a direction  $\delta\varphi$  as

$$\left( \nabla \tilde{\mathcal{J}}, \delta\varphi \right) \approx \frac{\tilde{\mathcal{J}}(\varphi + \alpha\delta\varphi) - \tilde{\mathcal{J}}(\varphi)}{\alpha}, \quad (\text{A34})$$

where  $\alpha$  is sufficiently small yet large enough to avoid round-off errors due to finite-precision floating-point arithmetic. In the current work,  $\alpha$  is chosen such that control perturbations are five orders of magnitude smaller than baseline controls. Approximating the full gradient  $\nabla \tilde{\mathcal{J}}$  would require evaluating Equation (A34) for as many linearly independent directions  $\delta\varphi$  as there are dimensions in  $\varphi$ . Here, we only evaluate a limited amount of gradient components, by choosing a set of pointwise unit perturbations  $\delta\varphi_i(t^*)$  to the baseline controls of each of the turbines  $i$  at different times  $t^*$ .

Figure A2 illustrates snapshots of both the forward and adjoint solutions at hub height. From Figure A2b it can be seen that the adjoint field starts out as streamtubes from the turbines indicating where immediate changes in the cost function originate, and transitions to a chaotic field after some upstream distance.

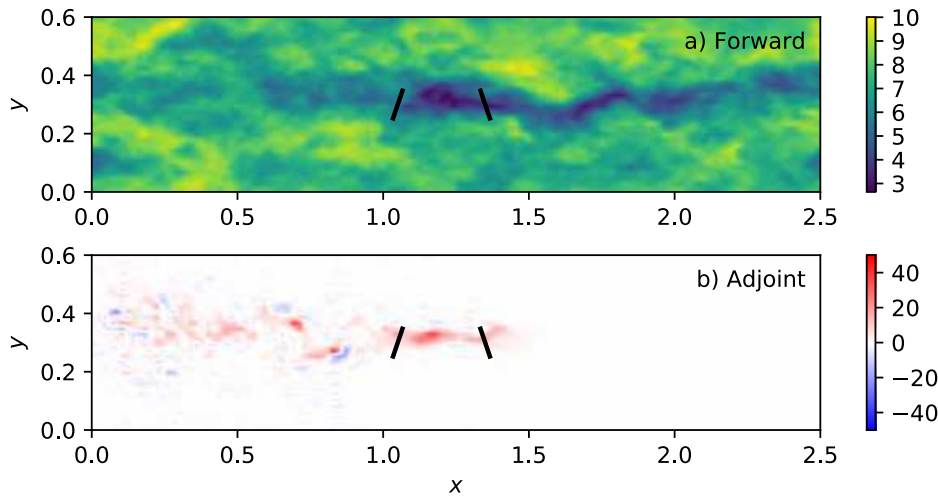


**Figure A2.** Solution fields for adjoint gradient verification test case at  $t = 150$  s. a) Forward field  $\tilde{u}_x$ . b) Adjoint field  $\xi_x$ .

Figure A3 illustrates the baseline controls  $\varphi$  around which the linearization is performed (Fig. A3a), as well as the adjoint gradient (full lines) compared to the finite difference gradient component approximations (dots) described above (Fig. A3b). It can be seen from the figure that the gradient approximations match well. The overall relative error between both remains below 5%. Note that, although this error could be further reduced through grid refinement, the current gradient accuracy is adequate for the optimizations considered in this work.

## References

1. Boersma, S.; Doekemeijer, B.; Gebraad, P.; Fleming, P.; Annoni, J.; Scholbrock, A.; Frederik, J.; van Wingerden, J. A tutorial on control-oriented modeling and control of wind farms. American Control Conference (ACC), 2017. IEEE, 2017, pp. 1–18.

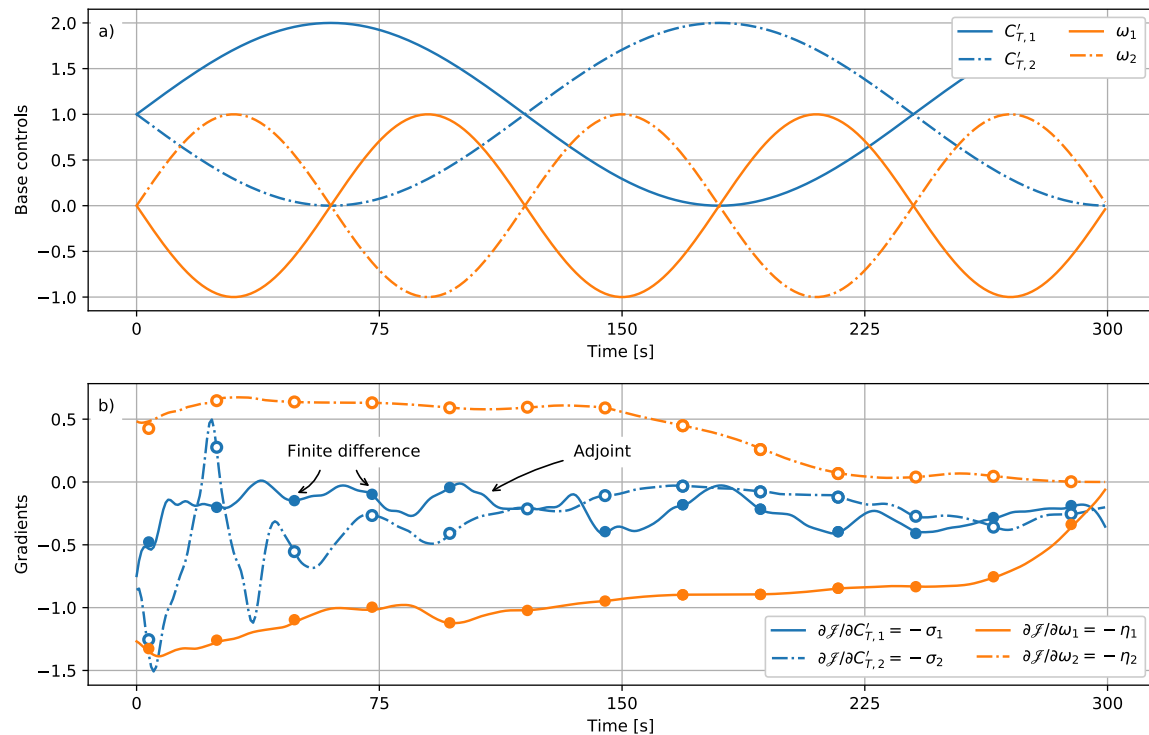


**Figure A3.** Adjoint gradient verification case. *a)* Baseline controls around which linearization is performed. *b)* Cost functional gradient. Full lines: adjoint, dots: finite-difference.

- 723 2. Knudsen, T.; Bak, T.; Svenstrup, M. Survey of wind farm control - power and fatigue optimization. *Wind*  
724 *Energy* **2015**, *18*, 1333–1351.
- 725 3. Annoni, J.; Gebraad, P.M.O.; Scholbrock, A.K.; Fleming, P.A.; Wingerden, J.W.v. Analysis of  
726 axial-induction-based wind plant control using an engineering and a high-order wind plant model. *Wind*  
727 *Energy* **2016**, *19*, 1135–1150. we.1891.
- 728 4. Steinbuch, M.; de Boer, W.; Bosgra, O.; Peters, S.; Ploeg, J. Optimal control of wind power plants. *Journal of*  
729 *Wind Engineering and Industrial Aerodynamics* **1988**, *27*, 237 – 246.
- 730 5. Horvat, T.; Spudić, V.; Baotić, M. Quasi-stationary optimal control for wind farm with closely spaced  
731 turbines. MIPRO, 2012 Proceedings of the 35th International Convention. IEEE, 2012, pp. 829–834.
- 732 6. Johnson, K.E.; Fritsch, G. Assessment of extremum seeking control for wind farm energy production. *Wind*  
733 *Engineering* **2012**, *36*, 701–715.
- 734 7. Gebraad, P.; Van Wingerden, J. Maximum power-point tracking control for wind farms. *Wind Energy* **2015**,  
735 *18*, 429–447.
- 736 8. Nilsson, K.; Ivanell, S.; Hansen, K.S.; Mikkelsen, R.; Sørensen, J.N.; Breton, S.P.; Henningson, D. Large-eddy  
737 simulations of the Lillgrund wind farm. *Wind Energy* **2015**, *18*, 449–467.
- 738 9. Campagnolo, F.; Petrović, V.; Bottasso, C.L.; Croce, A. Wind tunnel testing of wake control strategies.  
739 American Control Conference (ACC), 2016. IEEE, 2016, pp. 513–518.
- 740 10. Bartl, J.; Sætran, L. Experimental testing of axial induction based control strategies for wake control and  
741 wind farm optimization. *Journal of Physics: Conference Series* **2016**, *753*, 032035.
- 742 11. Goit, J.P.; Meyers, J. Optimal control of energy extraction in wind-farm boundary layers. *J Fluid Mech* **2015**,  
743 *768*, 5–50.
- 744 12. Goit, J.P.; Munters, W.; Meyers, J. Optimal Coordinated Control of Power Extraction in LES of a Wind Farm  
745 with Entrance Effects. *Energies* **2016**, *9*, 29.
- 746 13. Munters, W.; Meyers, J. Effect of wind turbine response time on optimal dynamic induction control of wind  
747 farms. *Journal of Physics: Conference Series* **2016**, *753*, 052007.

- 748 14. Munters, W.; Meyers, J. An optimal control framework for dynamic induction control of wind farms and  
749 their interaction with the atmospheric boundary layer. *Philos T Roy Soc A* **2017**.
- 750 15. Fleming, P.A.; Gebraad, P.M.; Lee, S.; van Wingerden, J.W.; Johnson, K.; Churchfield, M.; Michalakes, J.;  
751 Spalart, P.; Moriarty, P. Evaluating techniques for redirecting turbine wakes using SOWFA. *Renewable  
752 Energy* **2014**, *70*, 211–218.
- 753 16. Bossanyi, E. Individual blade pitch control for load reduction. *Wind energy* **2003**, *6*, 119–128.
- 754 17. Fleming, P.; Gebraad, P.M.; Lee, S.; van Wingerden, J.W.; Johnson, K.; Churchfield, M.; Michalakes, J.;  
755 Spalart, P.; Moriarty, P. Simulation comparison of wake mitigation control strategies for a two-turbine case.  
756 *Wind Energy* **2015**, *18*, 2135–2143.
- 757 18. VerHulst, C.; Meneveau, C. Altering kinetic energy entrainment in large eddy simulations of large wind  
758 farms using unconventional wind turbine actuator forcing. *Energies* **2015**, *8*, 370–386.
- 759 19. Clayton, B.; Filby, P. Measured effects of oblique flows and change in blade pitch angle on performance and  
760 wake development of model wind turbines. Proceedings of the 4th BWEA Wind Energy Conference, 1982,  
761 Vol. 13, pp. 559–572.
- 762 20. Grant, I.; Parkin, P.; Wang, X. Optical vortex tracking studies of a horizontal axis wind turbine in yaw using  
763 laser-sheet flow visualisation. *Experiments in Fluids* **1997**, *23*, 513–519.
- 764 21. Medici, D.; Alfredsson, P.H. Measurements behind model wind turbines: further evidence of wake  
765 meandering. *Wind Energy* **2008**, *11*, 211–217.
- 766 22. Bastankhah, M.; Porté-Agel, F. Experimental and theoretical study of wind turbine wakes in yawed  
767 conditions. *Journal of Fluid Mechanics* **2016**, *806*, 506–541.
- 768 23. Jiménez, Á.; Crespo, A.; Migoya, E. Application of a LES technique to characterize the wake deflection of a  
769 wind turbine in yaw. *Wind energy* **2010**, *13*, 559–572.
- 770 24. Howland, M.F.; Bossuyt, J.; Martínez-Tossas, L.A.; Meyers, J.; Meneveau, C. Wake structure in actuator  
771 disk models of wind turbines in yaw under uniform inflow conditions. *Journal of Renewable and Sustainable  
772 Energy* **2016**, *8*, 043301.
- 773 25. Gebraad, P.; Teeuwisse, F.; Wingerden, J.; Fleming, P.A.; Ruben, S.; Marden, J.; Pao, L. Wind plant power  
774 optimization through yaw control using a parametric model for wake effects - a CFD simulation study.  
775 *Wind Energy* **2016**, *19*, 95–114.
- 776 26. Quick, J.; Annoni, J.; King, R.; Dykes, K.; Fleming, P.; Ning, A. Optimization Under Uncertainty for Wake  
777 Steering Strategies. *Journal of Physics: Conference Series* **2017**, *854*, 012036.
- 778 27. Campagnolo, F.; Petrović, V.; Schreiber, J.; Nanos, E.M.; Croce, A.; Bottasso, C.L. Wind tunnel testing of a  
779 closed-loop wake deflection controller for wind farm power maximization. *Journal of Physics: Conference  
780 Series* **2016**, *753*, 032006.
- 781 28. Park, J.; Kwon, S.D.; Law, K. A Data-Driven, Cooperative Approach for Wind Farm Control: A Wind  
782 Tunnel Experimentation. *Energies* **2017**, *10*.
- 783 29. Soleimanzadeh, M.; Wisniewski, R.; Brand, A. State-space representation of the wind flow model in wind  
784 farms. *Wind Energy* **2014**, *17*, 627–639.
- 785 30. Fleming, P.; Annoni, J.; Shah, J.J.; Wang, L.; Ananthan, S.; Zhang, Z.; Hutchings, K.; Wang, P.; Chen, W.;  
786 Chen, L. Field test of wake steering at an offshore wind farm. *Wind Energy Science* **2017**, *2*, 229–239.
- 787 31. Gebraad, P.M.; Fleming, P.A.; van Wingerden, J.W. Wind turbine wake estimation and control using  
788 FLORIDyn, a control-oriented dynamic wind plant model. American Control Conference (ACC), 2015.  
789 IEEE, 2015, pp. 1702–1708.
- 790 32. Park, J.; Law, K.H. Cooperative wind turbine control for maximizing wind farm power using sequential  
791 convex programming. *Energy Conversion and Management* **2015**, *101*, 295–316.
- 792 33. Park, J.; Law, K.H. A data-driven, cooperative wind farm control to maximize the total power production.  
793 *Applied Energy* **2016**, *165*, 151 – 165.
- 794 34. Delport, S.; Baelmans, M.; Meyers, J. Constrained optimization of turbulent mixing-layer evolution. *Journal  
795 of Turbulence* **2009**, *10*, N18.
- 796 35. Nita, C.; Vandewalle, S.; Meyers, J. On the efficiency of gradient based optimization algorithms for  
797 DNS-based optimal control in a turbulent channel flow. *Computers & Fluids* **2016**, *125*, 11–24.
- 798 36. Munters, W.; Meneveau, C.; Meyers, J. Turbulent Inflow Precursor Method with Time-Varying Direction  
799 for Large-Eddy Simulations and Applications to Wind Farms. *Boundary-Layer Meteorol* **2016**, *159*, 305–328.

- 800 37. Meyers, J.; Sagaut, P. Evaluation of Smagorinsky variants in large-eddy simulations of wall-resolved plane  
801 channel flows. *Phys Fluids* **2007**, *19*, 095105.
- 802 38. Meyers, J.; Meneveau, C. Large eddy simulations of large wind-turbine arrays in the atmospheric boundary  
803 layer. *AIAA Paper* **2010**, *827*, 2010.
- 804 39. Calaf, M.; Meneveau, C.; Meyers, J. Large eddy simulation study of fully developed wind-turbine array  
805 boundary layers. *Phys Fluids* **2010**, *22*, 015110.
- 806 40. Byrd, R.H.; Lu, P.; Nocedal, J.; Zhu, C. A limited memory algorithm for bound constrained optimization.  
807 *SIAM Journal on Scientific Computing* **1995**, *16*, 1190–1208.
- 808 41. Wolfe, P. Convergence conditions for ascent methods. *SIAM review* **1969**, *11*, 226–235.
- 809 42. Jameson, A. Aerodynamic design via control theory. *Journal of Scientific Computing* **1988**, *3*, 233–260.
- 810 43. Giles, M.B.; Pierce, N.A. An introduction to the adjoint approach to design. *Flow, turbulence and combustion*  
811 **2000**, *65*, 393–415.
- 812 44. Tröltzsch, F. Optimal control of partial differential equations. *Graduate studies in mathematics* **2010**, *112*.
- 813 45. Borzì, A.; Schulz, V. *Computational optimization of systems governed by partial differential equations*; SIAM, 2011.
- 814 46. Bewley, T.R.; Moin, P.; Temam, R. DNS-based predictive control of turbulence: an optimal benchmark for  
815 feedback algorithms. *Journal of Fluid Mechanics* **2001**, *447*, 179–225.
- 816 47. Choi, H.; Hinze, M.; Kunisch, K. Instantaneous control of backward-facing step flows. *Applied Numerical  
817 Mathematics* **1999**, *31*, 133–158.
- 818 48. Munters, W.; Meneveau, C.; Meyers, J. Shifted periodic boundary conditions for simulations of  
819 wall-bounded turbulent flows. *Phys Fluids* **2016**, *28*.
- 820 49. Larsen, G.; Larsen, T.; Aagaard Madsen, H.; Mann, J.; Pena Diaz, A.; Barthelmie, R.; Jensen, L., The  
821 dependence of wake losses on atmospheric stability characteristics. In *Extended Abstracts*; Crespo, A.;  
822 Larsen, G.; Migoya, E., Eds.; Universidad Politecnica de Madrid, 2009; pp. 35–37.
- 823 50. Machefaux, E.; Larsen, G.C.; Koblitz, T.; Troldborg, N.; Kelly, M.C.; Chougule, A.; Hansen, K.S.; Rodrigo,  
824 J.S. An experimental and numerical study of the atmospheric stability impact on wind turbine wakes. *Wind  
825 Energy* **2016**, *19*, 1785–1805. we.1950.
- 826 51. Jonkman, J.; Butterfield, S.; Musial, W.; Scott, G. Definition of a 5-MW reference wind turbine for offshore  
827 system development. Technical Report Technical Report NREL/TP-500-38060, National Renewable Energy  
828 Laboratory, Golden, CO, USA, 2009.
- 829 52. Kooijman, H.; Lindenburg, C.; Winkelhaar, D.; van der Hooft, E. DOWEC 6 MW PRE-DESIGN: Aero-elastic  
830 modelling of the DOWEC 6 MW pre-design in PHATAS. Technical report, Energy Research Center of the  
831 Netherlands (ECN), 2003.
- 832 53. Kim, M.G.; Dalhoff, P.H. Yaw Systems for wind turbines – Overview of concepts, current challenges and  
833 design methods. *Journal of Physics: Conference Series* **2014**, *524*, 012086.
- 834 54. Munters, W. Large-eddy simulations and optimal coordinated control of wind-farm boundary layers. PhD  
835 thesis, KU Leuven, 2017.
- 836 55. Howard, K.B.; Singh, A.; Sotiropoulos, F.; Guala, M. On the statistics of wind turbine wake meandering:  
837 An experimental investigation. *Physics of Fluids* **2015**, *27*, 075103, [<http://dx.doi.org/10.1063/1.4923334>].
- 838 56. Allaerts, D.; Meyers, J. Boundary-layer development and gravity waves in conventionally neutral wind  
839 farms. *Journal of Fluid Mechanics* **2017**, *814*, 95–130.
- 840 57. Cal, R.B.; Lebrón, J.; Castillo, L.; Kang, H.S.; Meneveau, C. Experimental study of the horizontally averaged  
841 flow structure in a model wind-turbine array boundary layer. *J Renewable Sustainable Energy* **2010**, *2*, 013106.
- 842 58. Barthelmie, R.; Hansen, O.F.; Enevoldsen, K.; Hojstrup, J.; Frandsen, S.; Pryor, S.; Larsen, S.; Motta, M.;  
843 Sanderhoff, P.; others. Ten years of meteorological measurements for offshore wind farms. *Journal of Solar  
844 Energy Engineering-Transactions of The ASME* **2005**, *127*, 170–176.
- 845 59. Barthelmie, R.J.; Hansen, K.; Frandsen, S.T.; Rathmann, O.; Schepers, J.; Schlez, W.; Phillips, J.; Rados, K.;  
846 Zervos, A.; Politis, E.; others. Modelling and measuring flow and wind turbine wakes in large wind farms  
847 offshore. *Wind Energy* **2009**, *12*, 431–444.
- 848 60. Hinze, M.; Pinna, R.; Ulbrich, M.; Ulbrich, S. *Optimization with PDE constraints*; Vol. 23, Springer Science  
849 & Business Media, 2008.

© 2017 by the authors. Submitted to *Energies* for possible open access publication under the terms and conditions of the Creative Commons Attribution (CC BY) license (<http://creativecommons.org/licenses/by/4.0/>).